Combustion and Flame 000 (2020) 1–17

Contents lists available at ScienceDirect

Combustion and Flame

journal homepage: www.elsevier.com/locate/combustflame

Pulsating detonative combustion in n-heptane/air mixtures under off-stoichiometric conditions

Majie Zhao[a], Zhuyin Ren[b,c], Huangwei Zhang[a,*]

[a] Department of Mechanical Engineering, National University of Singapore, 9 Engineering Drive 1, Singapore 117576, Singapore
[b] Center for Combustion Energy, Tsinghua University, Beijing, China
[c] Institute for Aero Engine, Tsinghua University, Beijing, China

ARTICLE INFO

Article history:
Received 30 June 2020
Revised 7 December 2020
Accepted 8 December 2020
Available online xxx

Keywords:
Pulsating detonation
Deflagration-to-detonation transition
Pulsating frequency
Detailed mechanism
Chemical explosive mode analysis
n-Heptane

ABSTRACT

Numerical simulations of one-dimensional pulsating detonation in off-stoichiometric *n*-heptane/air mixtures are conducted by solving the reactive Navier–Stokes equations with a skeletal chemical mechanism. The effects of mixture equivalence ratio, initial pressure and temperature on pulsating detonations are studied. The results show that the pulsating instabilities in *n*-heptane/air mixtures are strongly affected by equivalence ratio. It is seen that pulsating instability only occurs in the fuel-lean or fuel-rich cases, whereas stable detonation is obtained for near-stoichiometric mixtures. Low-frequency pulsating detonations with single mode are observed, and decoupling / coupling of the reaction front and leading shock front occur periodically during the pulsating detonation propagation. The heat release and flame structure at the reaction front of the fuel-lean case differ from those in the fuel-rich case, and thus affects the DDT process of the reaction front. The pulsating detonation frequency is considerably influenced by equivalence ratio, initial pressure and temperature. The results of chemical explosive mode analysis and budget analysis of energy equation reveal that the mixture between the reaction front and shock front is highly explosive and thermal diffusion would promote the periodic dynamics of the reaction front and shock front. It is also found that the chemical explosion mode in the induction zone consists of two parts, i.e. the autoignition dominated reaction immediately behind the leading shock front and a following propagating reaction front.

1. Introduction

Detonation wave is the confluence of a self-sustained shock wave followed by an intense chemical reaction zone. For a stable detonation wave, the one-dimensional (1D) structure can be described with the Zeldovich [1], von Neumann [2] and Doring [3] (ZND) model. However, the classical steady ZND structure cannot be experimentally observed. Instead, a substantial body of literature [4–14] demonstrates that detonations are temporally and spatially unstable in nature, depending on initial conditions and mixture properties. The unstable patterns are manifested by periodic longitudinal variations of the self-sustained front with coupled shock wave and reaction zone, which is also called as pulsating or galloping detonation. They are found to be associated with the multi-dimensional cellular structures in practical situations. Therefore, it is of great relevance to study the 1D unstable detonation to unveil the complicated dynamics in multi-dimensional problems.

Unstable detonation is first observed experimentally by Campbell and Woodhead [15], which is further studied by Erpenbeck via linear / non-linear stability analysis [16–18] as well as Fickett and Wood using a numerical method [19]. Since then, detonation instability has been extensively investigated theoretically and computationally [5,10,20–27]. For instance, McVey and Toong [24] propose a wave-interaction theory for regular (or high-frequency) pulsating detonation, and their work shows that the leading shock and thin exothermic reaction zone are separated by a thermally neutral induction zone. The detonation instability is caused by the periodic interactions between leading shock and complicated wave structures (e.g. reaction shock, rarefaction wave and contact discontinuity) due to the new reaction front in the induction zone [24]. This mechanism is used by Daimon and Matsuo [25] to interpret the effects of overdrive degree ($f = D^2/D_{CJ}^2$, where D is the detonation velocity and the subscript “CJ” means Chapman——Jouguet state) on pulsating instability. It is also found that pulsating detonation occurs when the degree of overdrive is decreased [10,21]. In addition to the interactions between the leading shock wave and reaction front, Matsuo and Fujiwara [26] find that the compression wave reflected from the stagnation point of the projectile surface

---

* Corresponding author.
E-mail address: huangwei.zhang@nus.edu.sg (H. Zhang).

https://doi.org/10.1016/j.combustflame.2020.12.012

toward the bow shock also plays an important role in inducing the instabilities.

Most of the above theoretical or numerical studies are performed with one-step chemical models. It is well known that such simplified chemical mechanisms cannot reproduce the practical detonation dynamics affected by the energetic intermediates and chain-branching reactions. With a two-step reaction model, Mastuo and Fujii capture the high- and low-frequency pulsating modes [28]. Short and Quirk [29] use three-step chain-branching kinetics for pulsating detonation and find that the chain-branching cross-over temperature is a bifurcation parameter in pulsating detonation. It is also seen that a bifurcation boundary between stable and unstable detonations may exist when the length ratio of the heat release zone and induction zone is of the same order of the activation energy in the induction zone [11,30]. Moreover, Ng et al. [31] propose a stability parameter to quantify the degree of temperature sensitivity in the induction zone multiplied by the length ratio of induction to reaction zone based on two-step kinetics.

Simulations of 1D unstable detonation with detailed chemistry are also available [10,12–14,32,33]. For instance, Radulescu et al. simulate the 1D pulsating acetylene-oxygen detonations with seven-step mechanism and discuss the effects of argon dilution on detonation instability [33]. Leung et al. [12] show that a well-defined induction zone in the chain-branching model would help to understand the physical mechanisms that govern the pulsating detonations. Sussman obtains the amplitude, frequency and mode of 1D pulsation detonations with detailed H_2/air mechanism and compare the results with shock-induced combustion around the projectile [34]. Propagation of one-dimensional detonation in H_2/air mixtures is studied with detailed chemistry by Yungster and Radhakrishnan [10]. It is observed that for low pressure condition (0.22 bar), the predicted pulsating frequency is close to that from the McVey–Toong wave-interaction theory [24]. However, for higher pressures (0.42 and 0.8 bar) and near-stoichiometric mixtures, the foregoing theory would overpredict the pulsating frequency due to the infinitely fast heat release. Daimon and Matsuo simulate one-dimensional H_2/air detonations with detailed chemistry and discuss high- and low-frequency mode and their underpinning mechanisms [35]. Moreover, the effects of species diffusion and argon dilution on pulsating H_2/O_2 detonation was studied by Han et al. with detailed chemistry [13,14]. It is also found that diffusion has a prominent role for highly unstable detonation due to the existence of the bulk unreacted hydrogen pocket [32].

In recent years, increased interests have been shown in pursuit of detonation propulsion technologies, such as pulse detonation engines and rotating detonation engines [36,37]. Their commercialization necessitates utilization of realistic hydrocarbon fuels. The chemical kinetics of the hydrocarbon fuels are featured by many intermediates or radicals with a wide range of characteristic timescales. How the complex chemical kinetics evolve and how the chemical reaction and gas dynamics mutually influence in the induction zone are still not clear. As one of the main components of gasoline, *n*-heptane has been widely used as a test fuel for various engines. In this work, we focus on the highly unsteady behaviors of the reaction and shock waves in the induction zone of pulsating *n*-heptane detonations, through detailed one-dimensional simulations and Chemical Explosive Mode Analysis (CEMA) [38]. The influence of equivalence ratio, initial pressure and temperature on the pulsating detonation will be discussed. The rest of the paper is organized as below. In Sections 2 and 3, governing equation and physical model are presented. The results are presented and discussed in Section 4, followed by the conclusions in Section 5.

2. Governing equation and numerical method

2.1. Governing equation

The governing equations of mass, momentum, energy, and species mass fraction, together with the ideal gas equation of state, are solved in this work. They are respectively written as

$$\frac{\partial \rho}{\partial t} + \nabla \cdot [\rho \mathbf{u}] = 0, \tag{1}$$

$$\frac{\partial (\rho \mathbf{u})}{\partial t} + \nabla \cdot [\mathbf{u}(\rho \mathbf{u})] + \nabla p + \nabla \cdot \mathbf{T} = 0, \tag{2}$$

$$\frac{\partial (\rho \boldsymbol{E})}{\partial t} + \nabla \cdot [\mathbf{u}(\rho \boldsymbol{E} + \boldsymbol{p})] + \nabla \cdot [\mathbf{T} \cdot \mathbf{u}] + \nabla \cdot \mathbf{q} = \dot{\omega}_T, \tag{3}$$

$$\frac{\partial (\rho Y_m)}{\partial t} + \nabla \cdot [\mathbf{u}(\rho Y_m)] + \nabla \cdot \mathbf{s_m} = \dot{\omega}_m, \ \ (m = 1, \ldots M-1), \tag{4}$$

$$p = \rho R T. \tag{5}$$

Here t is time and $\nabla \cdot (\cdot)$ is divergence operator. ρ is the density, $\mathbf{u}$ is the velocity vector, p is the pressure and updated from the equation of state (i.e. Eq. (5)), and T is the temperature. Y_m is the mass fraction of m-th species, and M is the total species number. Only $(M-1)$ equations are solved in Eq. (4) and the mass fraction of the inert species (e.g. nitrogen) can be obtained from $\sum_{m=1}^{M} Y_m = 1$. $\boldsymbol{E}$ is the total energy, which is defined as $\boldsymbol{E} \equiv e + |\mathbf{u}|^2/2$. e is the specific internal energy and is defined as $e \equiv h_s - p/\rho$. Here $h_s \equiv \int_{T_0}^{T} C_p dT$ is the sensible enthalpy, and the temperature T is calculated from the solved h_s by Newton–Raphson method. $C_p = \sum_{m=1}^{M} Y_m C_{p,m}$ is the heat capacity at constant pressure, and $C_{p,m}$ is the heat capacity at constant pressure of m-th species, which can be estimated from JANAF polynomials [39]. R in Eq. (5) is the specific gas constant and calculated from $R = R_u \sum_{m=1}^{M} Y_m MW_m^{-1}$. MW_m is the molar weight of m-th species and R_u is universal gas constant.

The viscous stress tensor $\mathbf{T}$ in Eq. (2) is modeled by

$$\mathbf{T} = -2\mu \mathrm{dev}(\mathbf{D}). \tag{6}$$

Here μ is dynamic viscosity, and is predicted using Sutherland's law, $\mu = A_s \sqrt{T}/(1 + T_S/T)$. Here $A_s = 1.67212 \times 10^{-6}$ kg/m · s · $\sqrt{\mathrm{K}}$ is the Sutherland coefficient, while $T_S = 170.672$ K is the Sutherland temperature. Moreover, $\mathbf{D} \equiv [\nabla \mathbf{u} + (\nabla \mathbf{u})^{\boldsymbol{T}}]/2$ is the deformation gradient tensor and its deviatoric component in Eq. (6), i.e. $\mathrm{dev}(\mathbf{D})$, is defined as $\mathrm{dev}(\mathbf{D}) \equiv \mathbf{D} - \mathrm{tr}(\mathbf{D})\mathbf{I}/3$ with $\mathbf{I}$ being the unit tensor.

In addition, $\mathbf{q}$ in Eq. (3) is the diffusive heat flux and can be represented by Fourier's law, i.e.

$$\mathbf{q} = -k \nabla T. \tag{7}$$

Note that heat transfer due to mass transfer (e.g. different heat contents of various species or Dufour effect) is not considered in this work. In Eq. (7), thermal conductivity k is estimated using the Eucken approximation [40], i.e. $k = \mu C_v (1.32 + 1.37 \cdot R/C_v)$, where C_v is the heat capacity at constant volume and derived from $C_v = C_p - R$.

In Eq. (4), $\mathbf{s_m} = -D_m \nabla(\rho Y_m)$ is the species mass flux. The mass diffusivity D_m can be derived from heat diffusivity $\alpha = k/\rho C_p$, through $D_m = \alpha / Le_m$. With unity Lewis number assumption (i.e. $Le_m = 1$), the mass diffusivity D_m is calculated through $D_m = k/\rho C_p$. Moreover, $\dot{\omega}_m$ is the net production rate of m-th species by all N reactions, and calculated from the reaction rate of each elementary reaction $\omega_{m,\ j}^{o}$, i.e.

$$\dot{\omega}_m = MW_m \sum_{j=1}^{N} \omega_{m,\ j}^{o}. \tag{8}$$

Here $\omega^o_{m,\ j}$ is calculated from

$$\omega^o_{m,\ j} = \left(\nu''_{m,j} - \nu'_{m,j}\right)\left\{K_{fj}\prod_{m=1}^{M}[X_m]^{\nu'_{m,j}} - K_{rj}\prod_{m=1}^{M}[X_m]^{\nu''_{m,j}}\right\}. \qquad (9)$$

$\nu''_{m,j}$ and $\nu'_{m,j}$ are the molar stoichiometric coefficients of m-th species in j-th reaction, respectively. K_{fj} and $K_{rj}$are the forward and reverse rates of j-th reaction, respectively. $[X_m]$ is molar concentration and can be calculated from $[X_m] = \rho Y_m / MW_m$. Also, the term $\dot{\omega}_T$ in Eq. (3) accounts for the heat release from chemical reactions and is estimated as $\dot{\omega}_T = -\sum_{m=1}^{M}\dot{\omega}_m \Delta h^o_{f,m}$. Here $\Delta h^o_{f,m}$ is the formation enthalpy of m-th species.

2.2. Numerical method

The governing equations, i.e. Eqs. (1)–(4), are discretized with cell-centered finite volume method and solved by a density-based solver, *RYrhoCentralFoam* [41], which is developed from the fully compressible flow solver *rhoCentralFoam* in OpenFOAM® 5.0 [42]. A second-order implicit backward method is employed to discretize unsteady terms. Second-order Godunov-type upwind-central scheme, i.e. the Kurganov, Noelle and Petrova (KNP) method [6], is used for calculating the numerical flux of the convective term in momentum equation, i.e. Eq. (2). van Leer limiter is adopted for correct flux calculations with KNP scheme. TVD scheme is used for the convective terms in the energy and species mass fraction equations to ensure the boundness of the scalars. Also, second-order central differencing scheme are applied for the diffusion terms in Eqs. (2)–(4).

The chemical source terms, $\dot{\omega}_m$ and $\dot{\omega}_T$ in Eqs. (3) and (4), are integrated with a stiff ordinary differential equation solver, i.e. Seulex solver [43]. A skeletal mechanism with 112 reactions and 44 species is used for n-heptane/air combustion [44]. It has been well validated and good agreements with experimental data and theoretical value are seen about ignition delay time (over a range of 2.8 to 44 bars) [44] and Chapman–Jouguet velocity [45]. This mechanism has also been applied in previous studies of n-heptane detonation [46,47].

The original compressible flow solver, *rhoCentralFoam* in OpenFOAM®, is validated by Greenshields et al. [48] and Zhang et al. [41] using various benchmark tests, e.g. one-dimensional Sod's shock tube problem, two-dimensional forward-facing step and supersonic jet flows. Their results show that the KNP method with van Leer limiter can capture shock waves accurately. Furthermore, the solver *RYrhoCentralFoam* developed for compressible reactive flows has been validated for detonative combustion problems [49–51], and good agreements are achieved about detonation cell size and propagation speed compared to the corresponding theoretical and/or experimental data. It has been successfully applied for rotating detonative combustion, including detonation wave instability and bifurcation in gaseous medium [50,52] and n-heptane spray rotating detonation [47]. Besides, similar solver based on *rhoCentralFoam* has also been used by Gutierrez Marcantoni et al. [53,54] for one- and two-dimensional detonations.

3. Physical problem and numerical implementation

In this work, 1D simulations are performed to investigate the pulsating detonation propagation in n-heptane/air mixtures under different mixture conditions. Figure 1 shows the schematic of one-dimensional detonation tube closed at the left and right ends. The initial gas is n-heptane/air premixtures with various parameters, including equivalence ratio ϕ, initial pressure p_0 and temperature T_0. The equivalence ratio effects on pulsating detonations are studied through varying ϕ from 0.4 to 4.0. Besides, this effect will also be examined under different initial pressures (i.e. 0.5, 1.0, 2.0 and 5.0 atm) and temperatures (i.e. 300, 350, 400, 450 and 500 K). It should be acknowledged that the n-heptane vapor pressure effect is not considered when the gaseous mixture composition is specified, since in some fuel-rich cases the n-heptane partial pressure slightly exceeds the corresponding saturated value.

Since the unsteady characteristics (e.g. pulsating period) of pulsating detonations are significantly affected by the conditions of the initial mixtures [13], the length of the 1D detonation tube L in Fig. 1 is accordingly adjusted in different cases, to ensure that sufficiently long detonation propagation is achieved and therefore lasting pulsation phenomenon is demonstrated. For example, under p_0=1 atm and T_0=300 K, the domain length L is 3 m for ϕ=0.7, whilst it is longer for leaner mixtures, e.g. 16 m for ϕ=0.4.

In this work, detonation is directly initiated using a hot spot (2 mm thick) with high pressure (110 atm) and temperature (2500 K) at the left end of the shock tube in Fig. 1. This method can mimic the practical detonation initiation process, since no moving pistons behind the detonation wave are needed. It is used by Yungster and Radhakrishnan [10,55] to successfully initiate the pulsating detonations in hydrogen/air and ethylene/air mixtures. Note that the conditions of the hot spot (hence degree of overdrive) may affect the detonation development [10], but this effect will not be particularly studied in this work. Here at both left and right boundaries of the domain in Fig. 1, the velocity is assumed to be zero, whereas zero-gradient conditions are enforced for all the rest variables. Based on our tests, velocity specification at left boundary has little effects on detonation propagation. Since the mixture ahead of the detonation wave or shock wave are in its quiescent state, the right boundary condition is irrelevant provided the shock remains within the domain.

The domain in Fig. 1 is discretized with uniform Cartesian cells. The mesh resolutions used in the present simulations aim to resolve the detailed detonation structures and its length scale can be estimated with the Half-Reaction Length (HRL) from the ZND structures. The ZND structures are calculated based on the same mechanisms as for 1D pulsating detonations [44] with Shock & Detonation Toolbox [56]. The HRL, $L_{1/2}$, is considered as the distance from leading shock front to the location with peak heat release [57]. The HRL as a function of n-heptane/air equivalence ratio, initial temperature and pressure is shown in Fig. 2. It can be found that the HRL is significantly affected by the equivalence ratio, initial pressure or temperature. For fixed pressure and temperature, the HRL first decreases and then increases with equivalence ratio. Besides, it decreases while the initial pressure or temperature increases. To sufficiently resolve the n-heptane/air detonation structures, the grid resolution of more than 60 cells/$L_{1/2}$ is used in our simulations. Meanwhile, the resolutions of 30 cells/$L_{1/2}$ and 120 cells/$L_{1/2}$ are also tested to confirm the mesh independence of our results, and the analysis is presented in Section 4.1.

4. Results and discussion

4.1. Sensitivity analysis

The effects of time and space resolutions on predictions of pulsating n-heptane/air detonations are first studied. A representative case with initial conditions of $(\phi, T_0,\ p_0) = (0.7,\ 300\ \text{K},\ 1\ \text{atm})$ is selected. Figure 3 shows the time histories of pressure at the leading shock front (or termed as shock pressure for brevity) with different mesh resolutions of about 30 cells/$L_{1/2}$, 60 cells/$L_{1/2}$ and 120 cells/$L_{1/2}$, respectively. It is seen from Fig. 3 that only stable detonation is captured with the mesh resolution of 30 cells/$L_{1/2}$. In spite of slight pressure variations within the shown period, no pulsating detonation occurs with this resolution. Instead, single-mode pulsating detonation is captured with the finer mesh sizes,

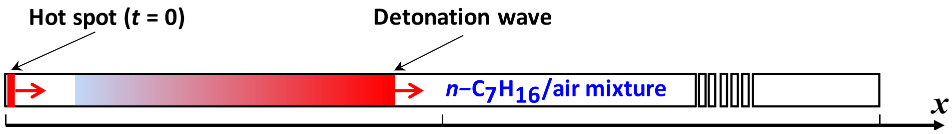

Fig. 1. Schematic of one-dimensional detonation tube. The initial gas is *n*-heptane/air premixtures.

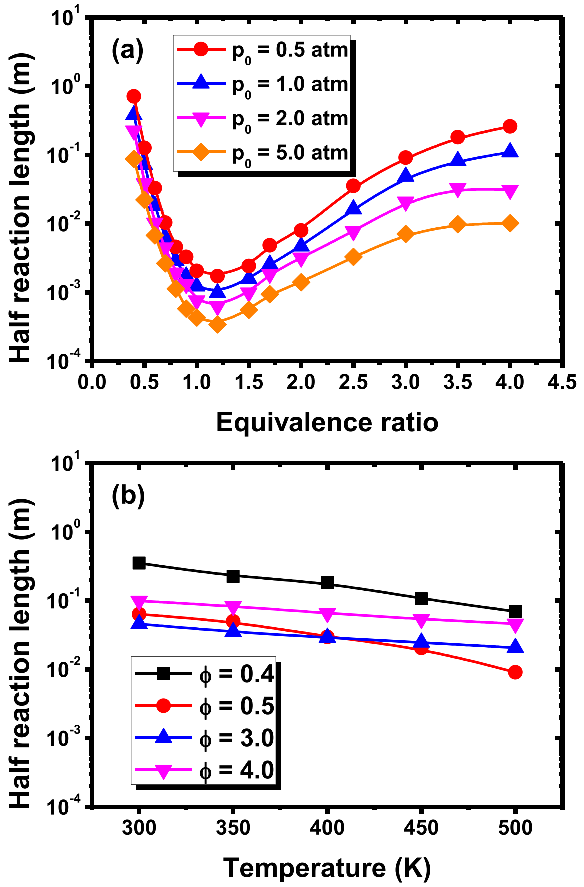

Fig. 2. Half-reaction length as a function of (a) *n*-heptane/air equivalence ratio (initial temperature: 300 K) and (b) initial temperature (initial pressure: 1 atm).

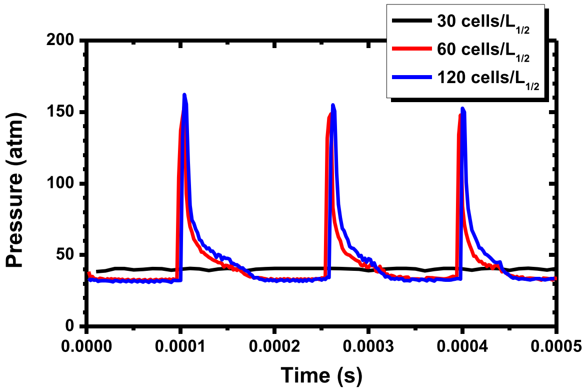

Fig. 3. Time history of shock pressure with different mesh sizes.

i.e. 60 cells/$L_{1/2}$ and 120 cells/$L_{1/2}$. Meanwhile, both pressure histories bear a close resemblance, except slightly faster pressure decreases in the result of 60 cells/$L_{1/2}$. Therefore, in light of the computational accuracy and cost, the cell size of 60 cells/$L_{1/2}$ is used for the simulations in this work. Moreover, quantitative assessment of the mesh resolution effects on detonation pulsating frequency will be shown in Appendix A.

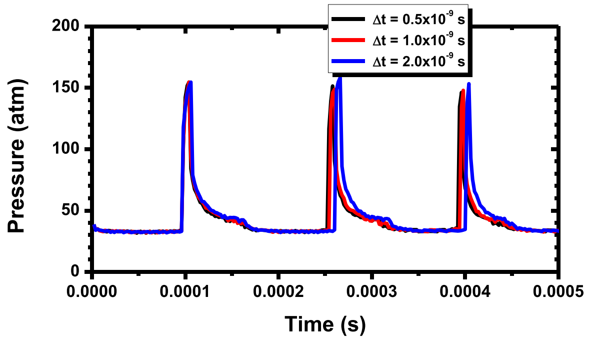

Fig. 4. Time history of shock pressure with different time steps.

Likewise, the influences of time step on the time histories of shock pressure in the same case are presented in Fig. 4. Three time steps, i.e. 2×10^{-9} s, 1×10^{-9} s and 0.5×10^{-9} s, are used for comparisons. One can see from Fig. 4 that variations of the time step show relatively small impact on the shock pressure variations in a pulsating detonation, in terms of peak value magnitude and intrinsic periodicity. Therefore, the time step of 1×10^{-9} s is used for the ensuing analysis.

4.2. Pulsating detonation in fuel-lean n-heptane/air mixtures

The temporal and spatial features of pulsating detonation in *n*-heptane/air mixture with initial conditions $(\phi, T_0, \ p_0) = (0.7, \ 300\text{ K}, \ 1\text{ atm})$ are demonstrated in Fig. 5. Figure 5(a) shows that the intensity of the leading shock changes periodically with the shock pressure varying between 30 atm to 125 atm and even above, leadings to the oscillation amplitude of $\Delta p/\bar{p} = 2.61$. Here Δp is the peak-to-trough shock pressure, whereas $\bar{p}$ is the average shock pressure (about 39 atm). The pressure oscillation frequency is $\omega = 6671$ Hz. Shock pressure oscillations are also seen previously from the hydrogen pulsating detonations, e.g. in Refs. [10,14,58]. However, the pulsation frequency in Fig. 5(a) is much lower than those work (above 1 MHz), indicating the low-frequency mode in this case. This similar mode is also reported by Yungster and Radhakrishnan [55] in their ethylene/air pulsating detonations. Regular variations of reaction front propagation velocity are observed with the oscillation amplitude of $\Delta D_{rf}/\bar{D}_{rf} = 0.51$, as demonstrated in Fig. 5(b). Here ΔD_{rf} is the peak-to-trough reaction front propagation speed, and $\bar{D}_{rf}$ is average propagation speed (about 1945 m/s). This is much higher than those (about 0.05) in the high-frequency H_2/air pulsating detonations, but close to those (about 0.09–0.49) in the low-frequency C_2H_4/air cases [55]. Meanwhile, both the computed average propagation speed and peak pressure in pulsating detonation are larger than the corresponding CJ speed (1672 m/s) and pressure (29 atm), which leads to the overdrive degree of $f = D^2/D_{CJ}^2 = 1.35$. Here D is the computed average detonation propagation speed from our simulation results. The overdrive is caused by the initiation hot spot with high pressure and temperature [10]. Regular low-frequency oscillations can also be found in the evolution of leading shock propagation speed (shown later in

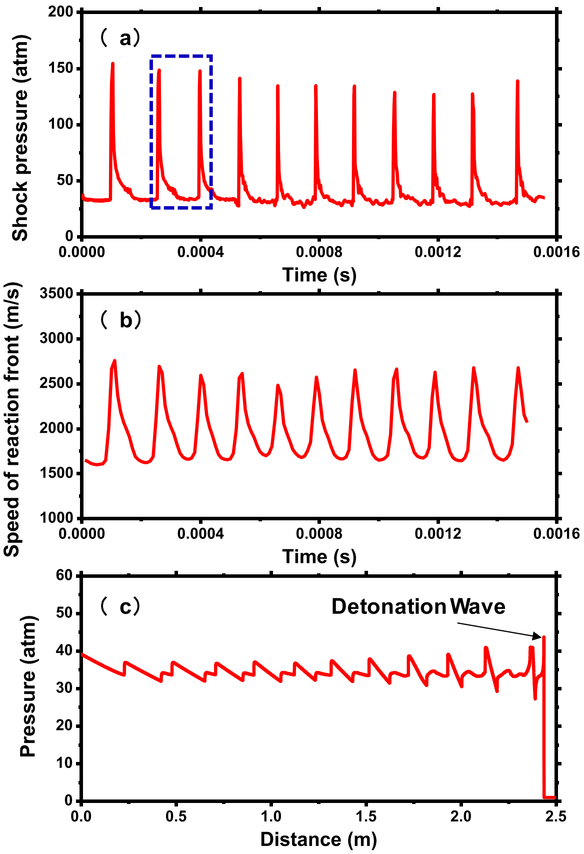

Fig. 5. Time history of (a) shock pressure and (b) reaction front propagation speed, and (c) spatial distribution of pressure. The initial condition is $(\phi, T_0,\ p_0) = (0.7,\ 300\ \mathrm{K},\ 1\ \mathrm{atm})$. The dashed box marks the period (0.24–0.43 ms) analyzed in Fig. 6.

Fig. 9). Furthermore, it is seen from Fig. 5(c) that behind the detonation wave (near $x = 2.5$ mm), galloped pressure fluctuations are present. This interesting phenomenon is related to the unsteady but periodic interaction of leading shock and reaction front and will be discussed further in Fig. 6.

Figure 6 shows the spatial and temporal distributions of temperature, pressure, formaldehyde (CH_2O), carbon monoxide (CO), density gradient and pressure gradient for the same case as in Fig. 5. Only their evolutions within one pulsating detonation cycle, i.e. 0.24–0.43 ms, are plotted, marked with a dashed box in Fig. 5(a). In this period, the reaction front (marked as *RF*) and shock front (i.e. *SF*) respectively show sequential and finitely long coupling (T_C) and decoupling (T_D) periods, as seen from Fig. 6(a). Here the coupling or decoupling instants are identified based on the distance between reaction and shock fronts [59]. If the distance is less than a small threshold (i.e. 1×10^{-8} m), they are deemed coupled, while if the distance is greater than the small threshold, they are decoupled. In Fig. 6, decoupling of the two fronts occurs at around 0.32 ms, and the coupling and decoupling periods, T_C and T_D, last about 0.06 ms and 0.08 ms, respectively. It is seen from Fig. 6(b) that the pressure of the leading shock *SF* is significantly elevated when *SF* is coupled with *RF* within the T_C period, while reduced when they are decoupled. This is consistent with the leading shock pressure variations presented in Fig. 5(a).

The dynamic behaviors of the shock front *SF* and reaction front *RF* within the decoupling period can be further discussed through pressure and density gradients, respectively in Fig. 6(c) and (d). Two bifurcations of the shock waves exist within the decoupling process, i.e. *B1* and *B2* in Fig. 6(d). The first bifurcation *B1* occurs at around 0.396 ms when a developing detonative front is formed in the shocked gas behind *SF*, and it is accompanied by formation of a series of compression waves (marked as "*CW*" in Fig. 6d) behind the reaction front. These compression waves further evolve into retonation shock wave while they propagate backward relative to the leading shock *SF*. The formation of the compression / shock waves (termed as "reaction shock" by Alpert and Toong [60]) is caused by rapid heat release around the detonative front. The second bifurcation *B2* occurs at around 0.402 ms when the detonative reaction front (generated from *B1*) overtakes the shock front, and it generates an expansion wave *EW*. The complex of compression / shock wave and expansion wave occurs periodically at the bifurcation loci *B1* and *B2* within each decoupling / coupling process, which well justifies the presence of the peculiar pressure spatial distribution in Fig. 5(c). Within the decoupling period T_D, a Deflagration-to-Detonation Transition (DDT) process occurs, which roughly ranges from the instant of the decoupling (marked as the dashed line between T_D and T_C in Fig. 6a) to the first pressure wave bifurcation point *B1*. After the foregoing process, a new puslating detonation cycle starts, as seen from Figs. 5. Therefore, periodic combustion surges between *SF* and *RF* are present in this low-frequency n-C_7H_{16}/air pulsating detonation, similar to the large-disturbance pulsating mode studied by Alpert and Toong [60] as well as by Mastuo et al. [35,61]. However, in the experiment [60], pulsating detonation is caused by traveling of the blunt projectile through a reactive gas at near-CJ speed and interacts with the shock waves reflected from the projectile surface.

The spatial and temporal variations of key species concentrations, such as CH_2O and CO, during the pulsating detonation process are shown in Fig. 6(e) and (f). It is shown that CH_2O is mainly distributed between the *RF* and *SF* in the decoupling period. Specifically, CH_2O concentration gradually increases with evolution of the *RF* before the first bifurcation *B1*. Then with the rapid consumption of CH_2O, the *RF* evolves into a detonation front. On the contrary, limited CH_2O is observed in the coupling period. As shown in Fig. 6(f), a large amount of CO is also produced near the *RF*, and its peak value has little change with the propagation of *RF*. Moreover, a secondary reaction front (*SRF* in Fig. 6c and d) can be clearly observed with relatively distributed CO concentration behind the *RF*. The temperature of the *SRF* is about 3000 K (see Fig. 6a), much higher than the *RF* temperature. The *SRF* stems from the continued chemical reactions of the un-detonated intermediate radicals.

To further elaborate the unsteady physics behind the above periodic variations of shock and reaction fronts, Fig. 7 shows the spatial distributions of pressure, temperature and heat release rate, corresponding to the same period in Fig. 6. The shock pressure first decreases from $t = 0.26$ ms (line #1) to 0.32 ms (line #4) within the coupling period T_C, accompanied by the apparent HRR reduction in Fig. 7(c). When the *RF* is decoupled with the leading *SF* from $t = 0.33$ ms (line #5) to 0.37 ms (line #7), the HRR from the *SF* is continuously reduced. In these instants, the locations of peak HRR slightly lag behind those of the *SF* (as indicated by the dashed line in Fig. 7b and c). Localized pressure rise can be found behind the leading *SF* at $t = 0.39$ ms (marked with red arrow), concurrently with increased heat release. This is also observed by Yungster and Radhakrishnan [10] in their calculations of hydrogen/air pulsating detonations. This pressure rise corresponds to the first bifurcation instant *B1* in Fig. 6. The *RF* penetrates into the leading *SF* at $t = 0.4$ ms (line #9), resulting in higher pressure (147 atm) and HRR (1.4×10^{14} J/m^3/s). The interaction between such high pressure and the shock front induces the second bifurcation *B2* at about 0.402 ms (see Fig. 6). The detonation wave propagates at an instantaneous speed of about 2600 m/s, much greater than the *C–J* speed of 1671 m/s. After $t = 0.4$ ms (e.g. line #10), the detonation wave continues propagating with coupled *RF* and *SF*. Meanwhile,

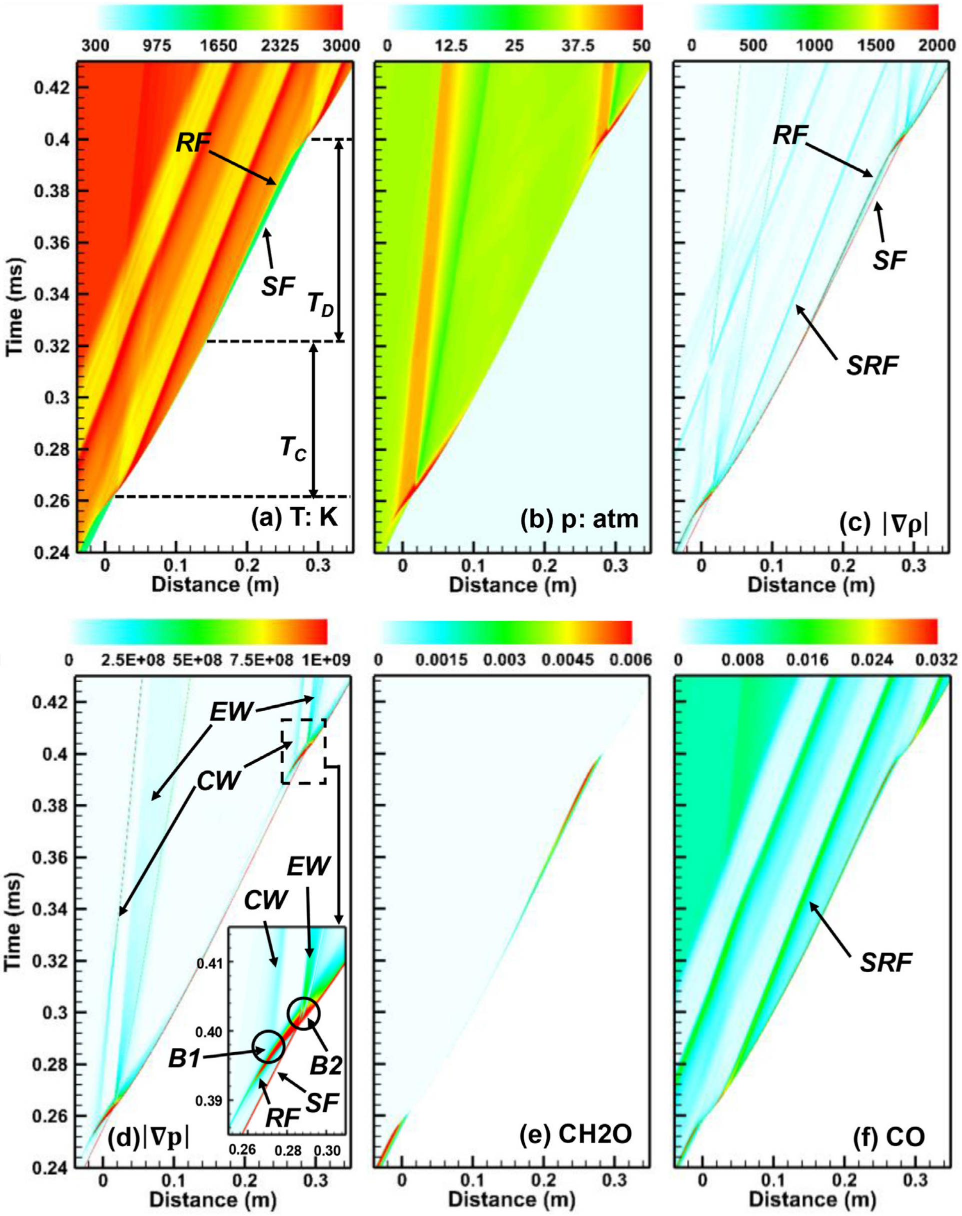

Fig. 6. Spatial and temporal distributions of (a) temperature (in K), (b) pressure (Pa), (c) density gradient (kg/m^4/s), (d) pressure gradient (Pa/s), (e) CH_2O and (d) CO. *RF*: reaction front; *SRF*: secondary reaction front; *SF*: shock front; *CW*: compression wave; *EW*: expansion wave; T_D: decoupling period; T_C: coupling period; *B1*, *B2*: bifurcation point.

the complex of compression / shock and expansion waves from *B1* and *B2* can be apparently seen from Fig. 7(a). This similar phenomenon, termed as “explosions in the explosion”, is also observed by Sharpe and Falle [22,62] in their calculations of 1D detonation, which is attributed to the pockets of partly burned fuels in the shocked gas when the activation temperature is high or constant energy addition by the piston. It may correspond to the “slow galloping” instability in square tubes [63,64], in which the detonation fails and decomposes into a flame decoupled from the leading shock. After an induction period it is re-initiated, and fails again, leading to a repeated process. Note that the transverse length or boundary of the shock tube would affect the pusating detonation propagation in experiments, e.g. [65], which is not included in the present one dimensional simualtions.

Likewise, the spatial distributions of C_2H_4, CH_2O, CO and OH mass fractions from the same pulsating detonation period as in Figs. 6 and 7 are shown in Fig. 8(a)–(d), respectively. Due to still high temperature (about 1300 K) between *RF* and *SF* when they are decoupled, the medium molecule pyrolytic products from *n*-heptane exist, such as C_2H_4 and CH_2O, and their peaks increase with time, i.e. from $t = 0.32$ ms (line #4) to $t = 0.39$ ms (line #8). Therefore, the heat release behind the leading shock front is mainly due to the oxidation of medium or small pyrolytic products by *n*-heptane, as evidenced by the rapidly reduced C_2H_4 and CH_2O, but increased CO and OH near the reaction front (marked with dashed lines in Fig. 8). However, they are very localized around the detonation wave and the concentrations are considerably reduced from $t = 0.39$ ms (line #8) to $t = 0.42$ ms (line #10). The accumulation of these species is expected to facilitate the formation of the auto-igniting spot with short excitation time at $t = 0.39$ ms (line #8), which is responsible for the new detonative spot and a series of compression waves as mentioned in Fig. 6.

Figure 9 shows the long-term evolutions of propagation speeds of the reaction and shock fronts in pulsating detonations in

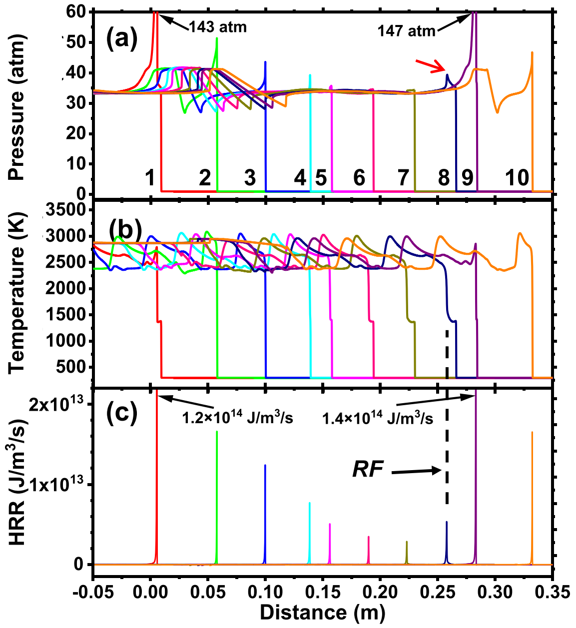

Fig. 7. Spatial profiles of (a) pressure, (b) temperature and (c) heat release rate. The time stamps for lines #1−#10 are: 1: 0.26 ms, 2: 0.28 ms, 3: 0.30 ms, 4: 0.32 ms, 5: 0.33 ms, 6: 0.35 ms, 7: 0.37 ms, 8: 0.39 ms, 9: 0.4 ms, 10: 0.42 ms. (For interpretation of the references to color in this figure, the reader is referred to the web version of this article.)

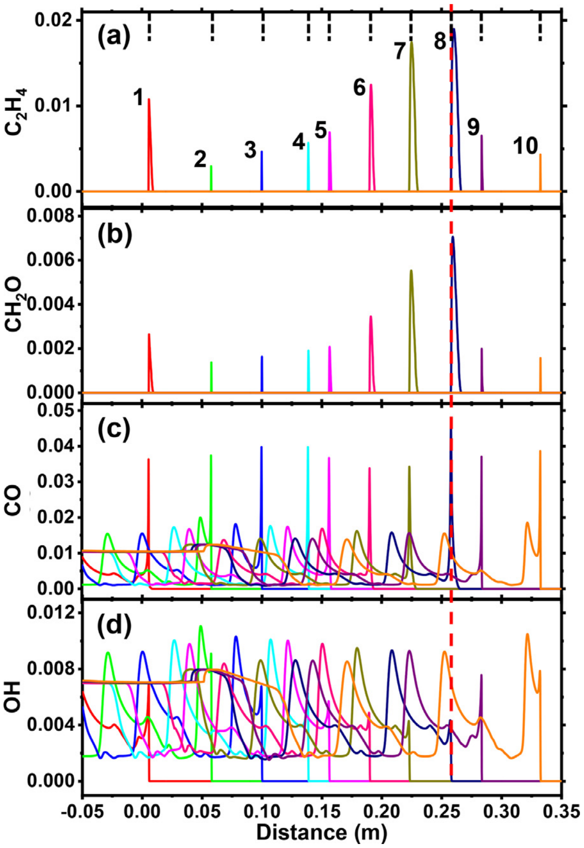

Fig. 8. Spatial profiles of (a) C_2H_4, (b) CH_2O, (c) CO and (d) OH mass fractions. The time stamps for labels #1−#10 are the same as in Fig. 7. Dashed lines: reaction front locations.

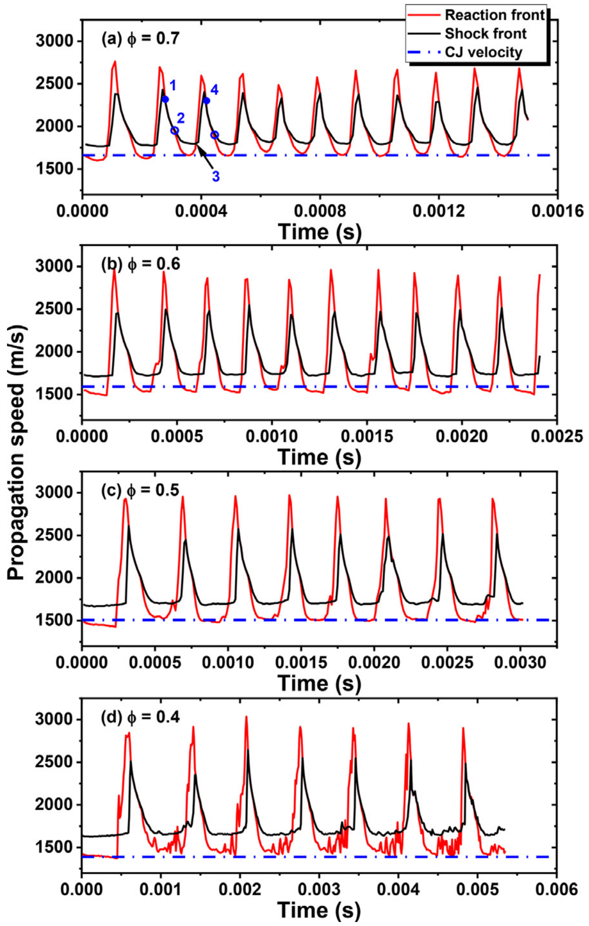

Fig. 9. Time histories of the propagation speeds of reaction and shock fronts for fuel-lean mixtures with equivalence ratios of (a) 0.7, (b) 0.6, (c) 0.5 and (d) 0.4. $T_0 = 300$ K and $p_0 = 1$ atm. Solid circles indicate the coupling instants for of the reactive and shock fronts, whereas the open circles the ones when the decoupling occurs. The dash-dotted lines denote the respective *C*−*J* velocities.

different fuel-lean mixtures. It is important to allow the detonation to run for sufficiently long to ensure that the complete pulsating detonation dynamics can be discovered [66]. The varying equivalence ratios include $\phi = 0.4$, 0.5, 0.6 and 0.7, whilst the initial pressure and temperature are fixed to be 1 atm and 300 K, respectively. Their degrees of overdrive are 1.62, 1.49, 1.41 and 1.37, respectively, for $\phi = 0.4$, 0.5, 0.6 and 0.7. The propagation speeds of the two fronts change periodically for all the shown equivalence ratios. No bifurcations leading to higher modes of instability are seen. Their speed variation amplitudes, $\Delta D_{rf}/\bar{D}_{rf}$ and $\Delta D_{sf}/\bar{D}_{sf}$, nearly do not change with ϕ and are 0.76 and 0.4, respectively. Meanwhile, within each pulsating detonation cycle, the increase of the *RF* speed is slightly earlier than that of the *SF* speed due to DDT.

Coupling of the two fronts is characterized by their equal speeds. For instance, the period between the instants 1 and 2 in Fig. 9(a) corresponds to synchronous propagation of the two coupled fronts, indicating detonative combustion. Note that in Fig. 7, the instants of $t = 0.28$ ms (line #2) and 0.30 ms (line #3) are in the coupling period, whereas $t = 0.32$ ms (line #4) is in the decoupling instant, i.e. instant 2 in Fig. 9. Nevertheless, within the duration between instants 2 and 4, two fronts are decoupled, featured by their distinct speeds. Scrutinizing of Fig. 9(a) reveals that this duration can be further divided into two stages, i.e. accelerated decoupling (i.e. 2−3) and accelerated coupling (i.e. 3−4) based on the relations of the *SF* and *RF* speeds. At instant 3 in Fig. 9(a), the speeds of the

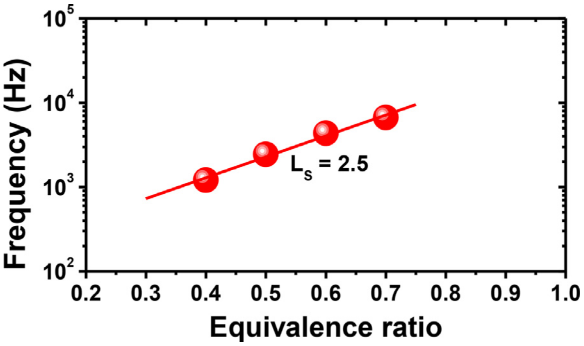

Fig. 10. Pulsation frequencies of the reaction front with equivalence ratios of 0.4, 0.5, 0.6 and 0.7. $T_0 = 300$ K and $p_0 = 1$ atm. Line: linear fitted curve with the slope of 2.5.

two fronts are the same. Accelerated decoupling is characterized by gradually increased distance between the *RF* and *SF*, while accelerated coupling corresponds to gradual approaching of the two traveling fronts. It is shown that the instants of 0.33 ms (line #5 in Fig. 7), 0.35 ms (line #6) and 0.37 ms (line #7) are in the accelerated decoupling stage, whilst the instants of 0.39 ms (line #8) and 0.40 ms (line #9) are in the accelerated coupling stage.

Moreover, it is seen from Fig. 9 that the pulsating frequency increases with equivalence ratio. It is found that the intervals between the deaths and re-ignition increases with activation temperature [21,22]. Figure 10 quantifies the exponential dependence of pulsating detonation frequencies ω on the equivalence ratio ϕ, and the slope of the fitted curve of $\log_{10}\omega$ versus ϕ is about 2.5. Note that here the frequency ω in Fig. 10 is from the reaction front and that of the leading shock is very close to it. For fuel-lean mixtures, when ϕ is 0.8 and 0.9, stable, instead of pulsating, detonations are observed in our simulations. Similar relations between ω and ϕ are also reported by Yungster and his co-workers in pusalting detonations of hydrogen/air [10] and ethylene/air [55] mixtures.

4.3. Pulsating detonation in fuel-rich n-heptane/air mixtures

Figure 11 shows the spatial and temporal distributions of temperature, pressure, CH_2O, CO, density gradient and pressure gradient for a fuel-rich *n*-heptane/air mixture with $\phi = 3.0$. The initial temperature and pressure are 300 K and 1 atm, respectively. One pulsation period is shown, from $t = 0.2$ ms to 0.36 ms. The transients observed in the fuel-lean case of $\phi = 0.7$ are also observed here, including coupling and decoupling of *RF* and *SF*, compressible and expansion waves from shock bifurcation, and secondary reaction front. However, there are still differences between the two cases. For instance, the CO and CH_2O concentrations between *SF* and *RF* in the fuel-rich mixture are much (almost one order of magnitude) higher than those with $\phi = 0.7$. Also, the duration of one pulsating detonation cycle (i.e. $T_D + T_C$) is about 0.108 ms, slightly shorter than that of the fuel-lean case in the last section, i.e. about 0.14 ms. Figure 11(a) also shows that the decoupling period accounts for 78% of the entire one, longer than that in the fuel-lean results, i.e. 57%, although the durations for decoupling period in two cases are close (about 0.08 ms). Moreover, inspection of Fig. 11(d) shows that a trifurcation point exists at $t = 0.294$ ms. At this point, a weak backward-propagating compression wave (*CW1* in the inset of Fig. 11d) and a strong forward-propagating compressible wave (*CW2*) relative to the *RF* are generated. After the trifurcation point, intense deflagration arises with increased pressure gradient along the *RF*. These compression waves are caused by the localized thermal runaway around the trifurcation point.

Figure 12 further shows the spatial distributions of temperature, HRR, mass fraction of C_2H_4, CH_2O and CO around the trifurcation point ($t = 0.3$ ms). Pressure curves are included for reference. In Fig. 12(a), the left- and right-propagating compressible waves, *CW1* and *CW2*, are clearly observed. Behind the *SF*, the temperature slightly decreases first due to the endothermic reactions for heavy hydrocarbon pyrolysis, and then gradually increases caused by the local chemical reactions. A pronounced temperature rise is observed at $x = 0.098$ m (dashed line in Fig. 12), arising from the intense deflagration with strong heat release as shown in Fig. 12(b). This reaction front would evolve into a new detonation wave, as seen in Fig. 11(c) and (d). CH_2O and C_2H_4 are generated behind the shock front *SF* and quickly consumed around the *RF* (see Fig. 12c), leading to sharply increased CO concentration (see Fig. 12d). This indicates that the heat release from the intense deflagration is mainly due to the oxidation of small hydrocarbon radicals, such as C_2H_4 and CH_2O.

Figure 13 shows the evolutions of pressure, temperature and HRR within the same pulsating detonation cycle in Fig. 11. Similar unsteady phenomena to those from the fuel-lean case in Fig. 7 are observed here. The leading shock pressure first decreases from $t = 0.22$ ms (line #1) to 0.25 ms (line #3) in the coupling period. The *RF* tends to decouple with the *SF*, manifested with decreased shock pressure and HRR from lines #1 to #3. In the decoupling period T_D (from lines #4 to #9), the leading shock pressure levels off for a finitely long time. The striking pressure increase occurs around the *RF* in the shocked gas since $t = 0.29$ ms (line #6), which is close to the trifurcation point discussed in Fig. 11. The *RF* pressure abruptly increases from $t = 0.30$ ms (line #7) to 0.330 ms (line #9), accompanied by the increasingly stronger HRR. This implies that the *SF* and *RF* are mutually enhanced, leading to the eventual formation of the new detonation front. The peak pressure of the new detonation wave is about 91 atm, much smaller than that in the fuel-lean case in Fig. 7, i.e. 147 atm. The new detonation wave accelerates and overtakes the preceding *SF* at $t = 0.34$ ms (line #10), which results in a detonation wave. Then the *RF* and *SF* start the next cycle of the pulsating detonation.

Figure 14 shows the profiles of C_2H_4, CH_2O, CO, and OH mass fractions corresponding to the same instants in Fig. 13. The medium molecule pyrolytic products by *n*-heptane, such as C_2H_4 and CH_2O, increase gradually in the DDT process (lines #3–#9), and then decrease rapidly after a new detonation is formed with coupled *RF* and *SF*. This is also seen from the results of $\phi = 0.7$. However, differently, the peak values of C_2H_4 and CH_2O is much greater than that in the fuel-lean case, as also found from Fig. 11. Although CH_2O behind the *SF* increases first and then decrease rapidly in the decoupling period, the peak value of CH_2O is located at the reaction front. Moreover, an increasing of CO at the reaction front is observed and no peak value of OH is observed near the reaction front. The temporal and spatial evolutions of these species between the *SF* and *RF* suggest that the DDT process of reaction front in fuel-rich case may have different dominant reaction paths compared to the fuel-lean case.

Figure 15 shows the long-term evolutions of propagation speeds of reaction and shock fronts in fuel-rich mixtures, i.e. $\phi = 2.0$, 2.5, 3.0 and 4.0. Apparently, propagation of *RF* and *SF* shows significant pulsating instabilities. The coupled (i.e. 1–2), accelerated decoupling (2–3) and accelerated coupling (3–4) propagations of the two fronts can also be identified, e.g. in Fig. 15(b), similar to the fuel-lean results in Fig. 9. The *RF* pulsating frequencies are shown in Fig. 16, and the pulsating frequency decreases exponentially with the increased equivalence ratios. The slope of the fitted curve is about −0.29, the magnitude of which is much smaller than that (about 2.5) for the fuel-lean case ($\phi = 0.7$) in Fig. 10. Therefore, the pulsating frequency in fuel-lean gas is more sensitive to equivalence ratio than in fuel-rich one. Moreover, low-frequency

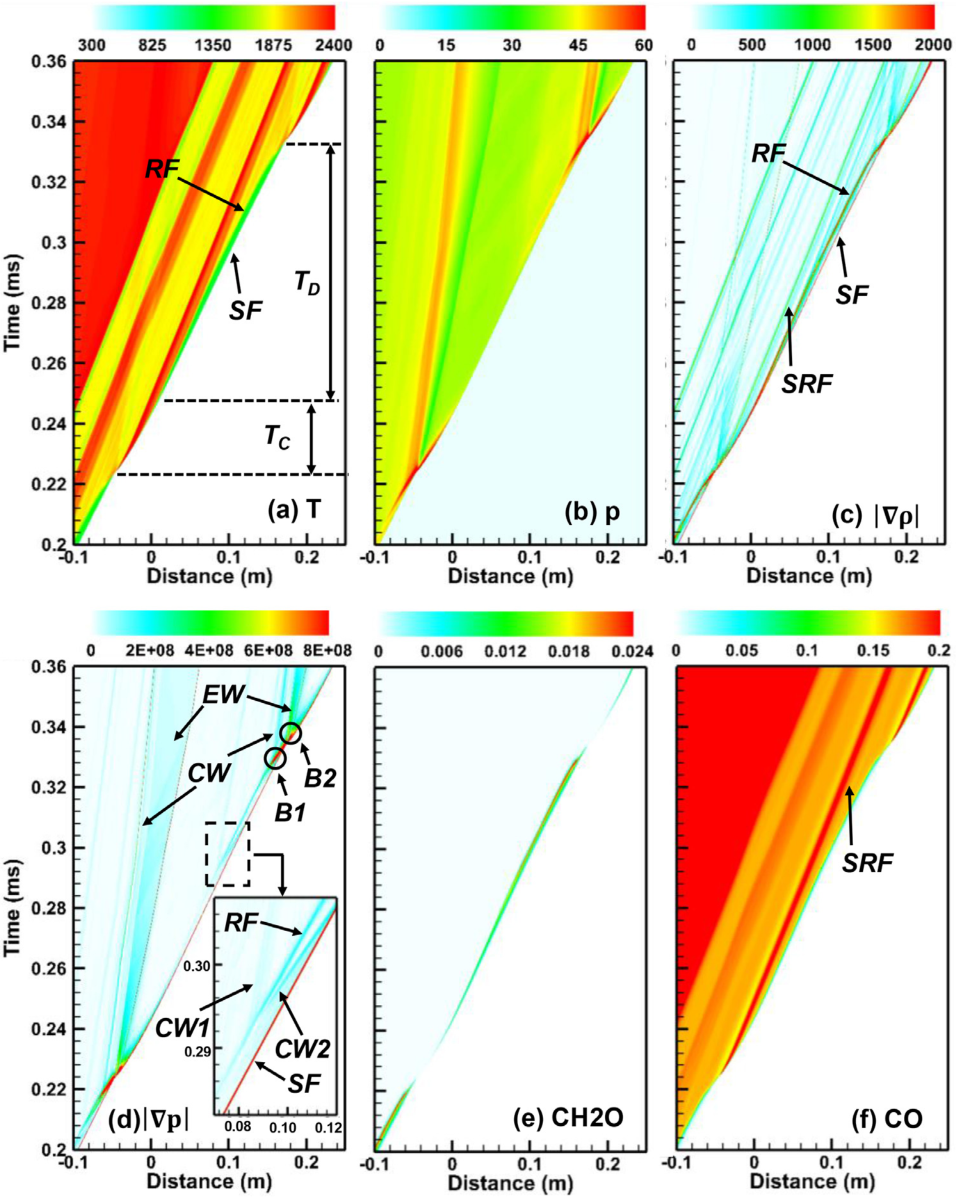

Fig. 11. Spatial and temporal distributions of (a) temperature (in K), (b) pressure (Pa), (c) density gradient (kg/m^4/s), (d) pressure gradient (Pa/s), (e) CH_2O and (d) CO. *RF*: reaction front; *SRF*: secondary reaction front; *SF*: shock front; *CW*, *CW1*, *CW2*: compression waves; *EW*: expansion wave; T_D: decoupling period; T_C: coupling period; *B1*, *B2*: bifurcation point.

pulsating detonations in fuel-rich ethylene/air mixtures are also predicted by Yungster and Radhakrishnan [55] (see Fig. 16). It is shown that the pulsating frequency of ethylene/air is higher than that of n-C_7H_{16}/air mixtures, but they have close slopes.

The pulsating *RF* and *SF* propagation speeds vary between 1600 and 3000 m/s, larger than the *C–J* velocity. Their speed variation amplitudes, $\Delta D_{rf}/\bar{D}_{rf} = 0.65$ and $\Delta D_{sf}/\bar{D}_{sf} = 0.42$, which are almost the same for the cases in Fig. 15. Meanwhile, the degrees of overdrive are 1.40, 1.51, 1.69 and 1.65 respectively for $\phi = 2.0$, 2.5, 3.0 and 4.0. It can also be found that the time of the DDT process for a new detonation increases with the increased equivalence ratios for fuel-rich cases. However, for fuel-lean cases as shown in Fig. 9, the time of the DDT process increases with the decreased equivalence ratios. Moreover, in fuel-rich mixtures, the *RF* propagation speed has a two-stage increase in the DDT process, particularly true for high equivalence ratios (e.g. 2.5–4.0 in Fig. 15b–d). We take $\phi = 3.0$ in Fig. 15(c) as an example. The first increase occurs around the trifurcation point, i.e. $t = 0.294$ ms, whilst the second occurs at the bifurcation *B1*, i.e. $t = 0.328$ ms (see Fig. 11d). This is not seen in the fuel-lean cases, in which only one increase of front propagation speeds at the bifurcation *B1* before the detonation is formed.

4.4. Effects of initial temperature and pressure

In Sections 4.2 and 4.3, the pulsating detonations in n-heptane/air mixtures are studied under the initial temperature of 300 K and initial pressure of 1 atm. Figure 17 shows the time histories of the reaction and shock front propagation speeds with various initial temperatures (300–500 K). The equivalence ratio is fixed to be $\phi = 3.0$, whilst the initial pressure is 1 atm. It can be found that the propagation speeds are much higher than the *C–J* velocity, and their degrees of overdrive are 1.69, 1.79, 1.73, 1.46 and 1.53 respectively for $T_0 = 300$, 350, 400, 450 and 500. Pulsating propagations of *RF* and *SF* are observed from 300 K to 400 K in Figs. 17(a)–17(c), and the pulsating frequencies ω increase with

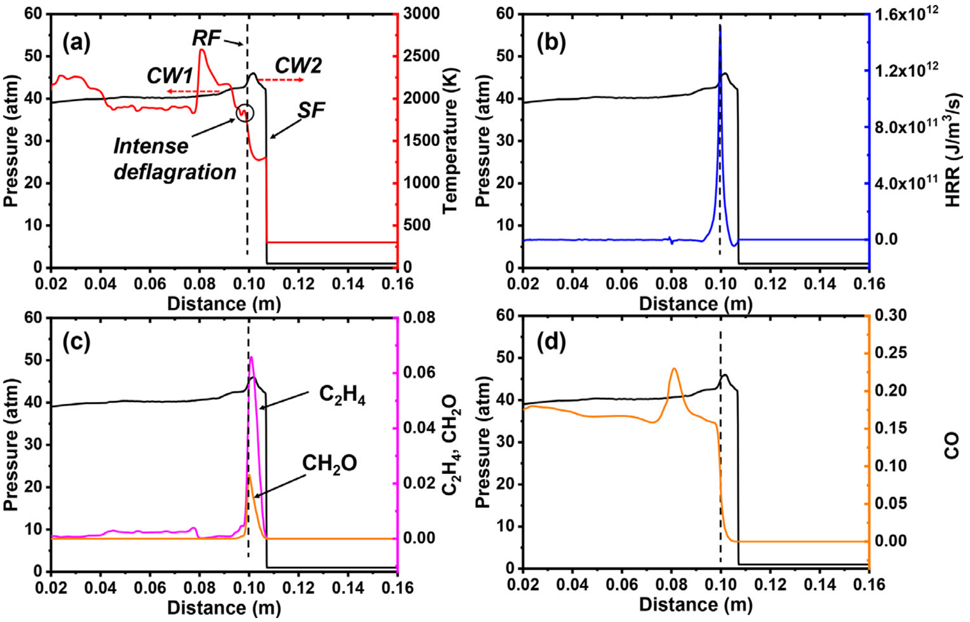

Fig. 12. Spatial profiles of (a) temperature, (b) heat release rate, mass fractions of (c) C_2H_4 and CH_2O and (d) CO at $t = 0.3$ ms. Dashed lines indicate the *RF* location. Implications for the abbreviations in (a) are listed in the caption of Fig. 11.

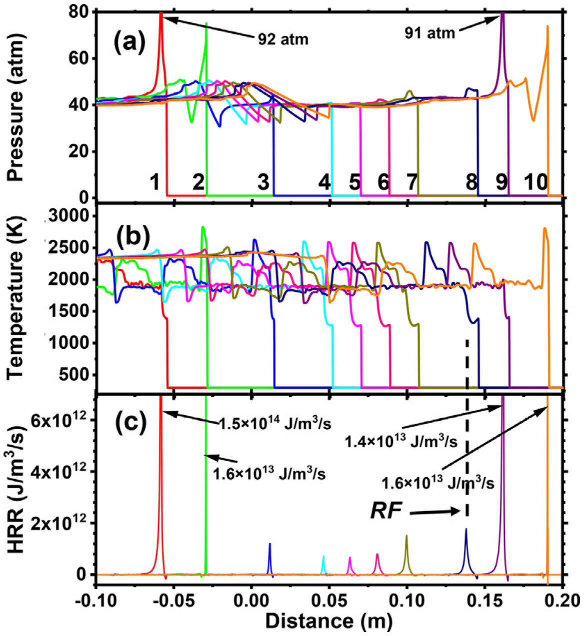

Fig. 13. Spatial profiles of (a) pressure, (b) temperature and (c) heat release rate. The time stamps for lines #1–#10 are: 1: 0.22 ms, 2: 0.23 ms, 3: 0.25 ms, 4: 0.27 ms, 5: 0.28 ms, 6: 0.29 ms, 7: 0.30 ms, 8: 0.32 ms, 9: 0.33 ms, 10: 0.34 ms.

increased T_0. Accordingly, durations of the alternate stages decrease, including coupling, accelerated and accelerated decoupling. In addition, the maximal propagation speed decreases as T_0 increases. As seen in Figs. 17(d) and 17(e), pulsating detonation disappears when T_0 is increased to 450 and 500 K; instead, only stable detonation with constant propagation speed occurs. Note that in both stable and pulsating detonations, the instantaneous propagation speeds of both fronts are consistently larger than the respective *C–J* values.

Besides $\phi = 3.0$ in Fig. 17, pulsating detonations are also studied for other equivalence ratios, i.e. $\phi = 0.4$, 0.5 and 4.0, with variable initial temperatures. The pulsating frequency ω of the reaction

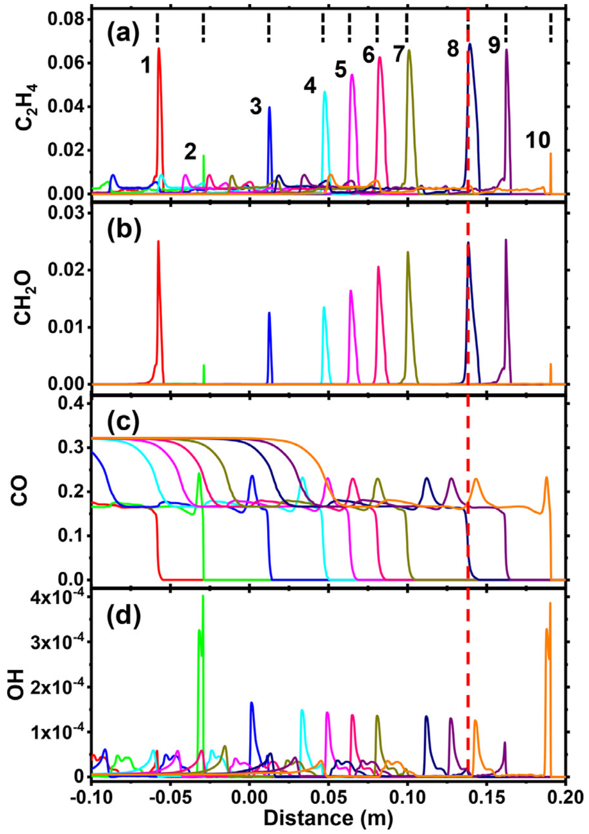

Fig. 14. Spatial profiles of (a) C_2H_4, (b) CH_2O, (c) CO and (d) OH mass fractions. The time stamps for labels #1–#10 are the same as in Fig. 13. Dashed lines: reaction front locations.

front with different initial temperatures T_0 are shown in Fig. 18. Generally, ω increases exponentially with increased T_0. However, pulsating detonations disappear with higher T_0 beyond the rightmost points for individual equivalence ratios in Fig. 18. For example, for $\phi = 0.4$, the pulsating instabilities occur when the initial

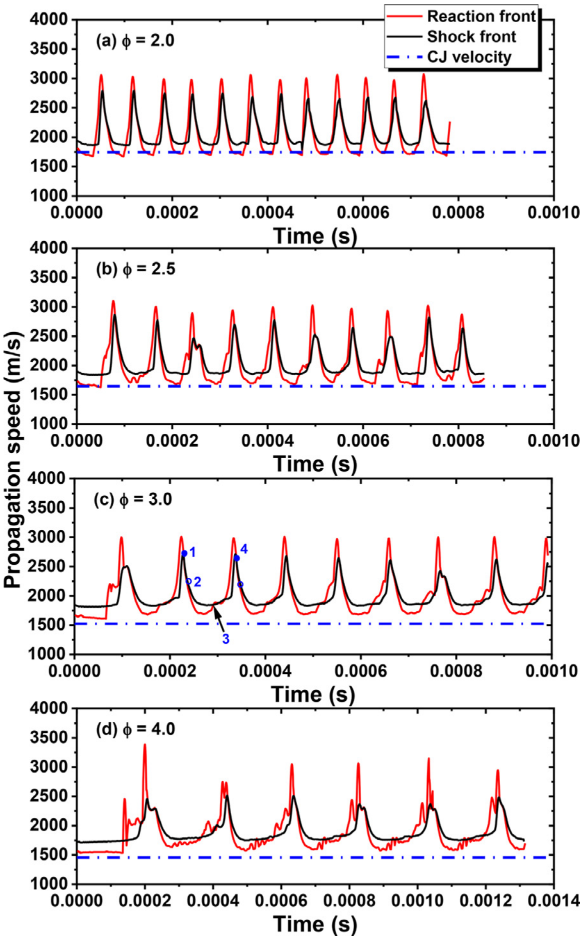

Fig. 15. Time histories of propagation speeds of the reaction and shock fronts for mixture equivalence ratios of (a) 2.0, (b) 2.5, (c) 3.0 and (d) 4.0. $T_0 = 300$ K and $p_0 = 1$ atm. Legend for the circles is same as in Fig. 9.

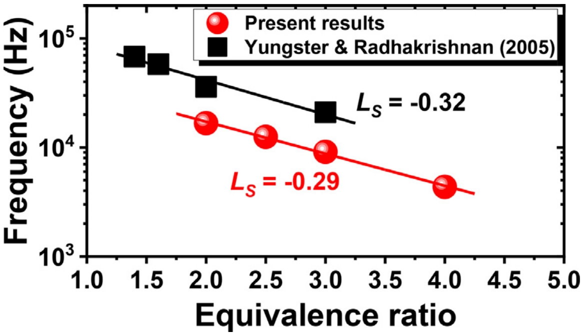

Fig. 16. Pulsation frequencies of the reaction front with mixture equivalence ratios of 2.0, 2.5, 3.0 and 4.0. $T_0 = 300$ K and $p_0 = 1$ atm. Line: linear fitted curves with the slopes of L_S. Black square: pulsating detonation frequency in ethylene/air mixtures [55].

temperatures $T_0 = 300$ K, 350 K and 400 K, but stable detonation is obtained with $T_0 = 450$ K and above. Generally, in both fuel-lean and fuel-rich cases, the dependence of pulsating frequency on the initial temperature has limited change with equivalence ratio. In the meantime, the pulsating frequencies of the fuel-lean cases are more sensitive to the initial mixture temperature than those of fuel-rich ones. These tendencies are clearly manifested by the relations between the slopes of various fitted curves in Fig. 18.

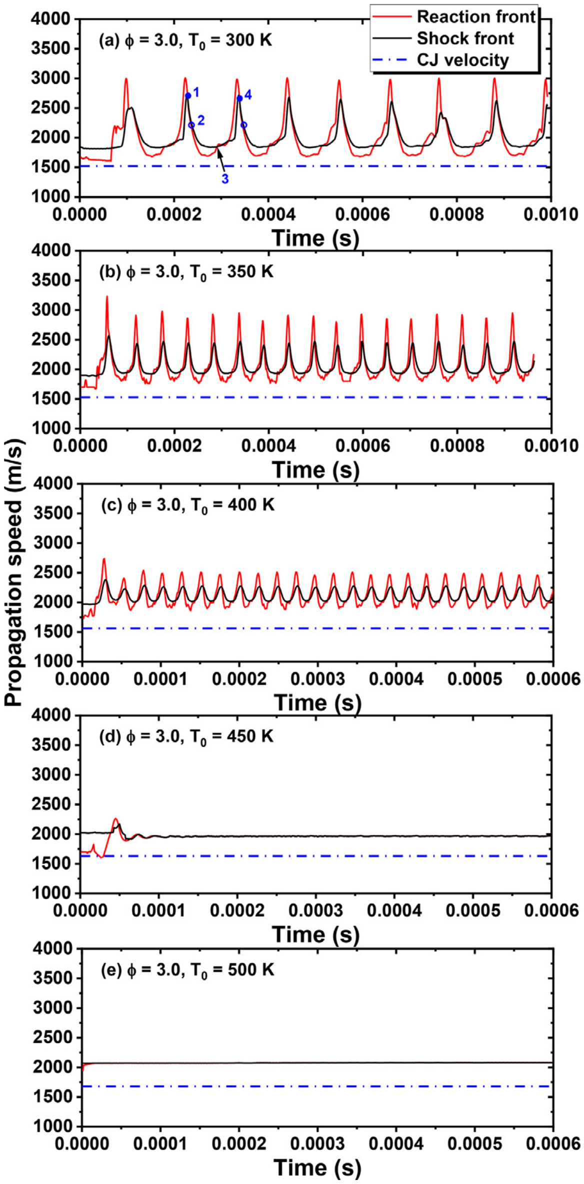

Fig. 17. Time histories of the reaction and shock front speeds with initial temperatures of (a) 300 K, (b) 350 K, (c) 400 K, (d) 450 K and (e) 500 K. The equivalence ratio is 3.0 and initial pressure is 1 atm. Legend for the circles is same as in Fig. 9.

The effects of initial pressure on the pulsation frequency are studied and Fig. 19 shows the pulsation frequencies ω of the reaction front with different initial pressures. The off-stoichiometric equivalence ratios range from 0.4 to 4.0 are studied. It should be highlighted that in the initial pressure range in Fig. 19, stable detonations with constant propagation speeds are obtained with near-stoichiometric n-heptane/air mixtures, e.g. $\phi = 0.8-1.5$. Apparently, ω increases linearly with initial pressure in all the studied equivalence ratios. The pulsation frequencies of the fuel-rich cases have stronger sensitivity to initial pressure than those of fuel-lean ones. It should be noted that the range of equivalence ratios for pulsating detonation does not change with the initial pressure. The exception is $\phi = 0.7$, with which pulsating detonation is only observed with $p_0 = 1.0$, 2.0 and 5.0 atm.

4.5. Chemical explosive mode analysis

In this Section, chemical explosive mode analysis [38], together with budget analysis of the energy equation (i.e. Eq. (3)), is conducted to identify the physics associated with pulsating n-C_7H_{16}/air detonation. CEMA has been proved as a reliable

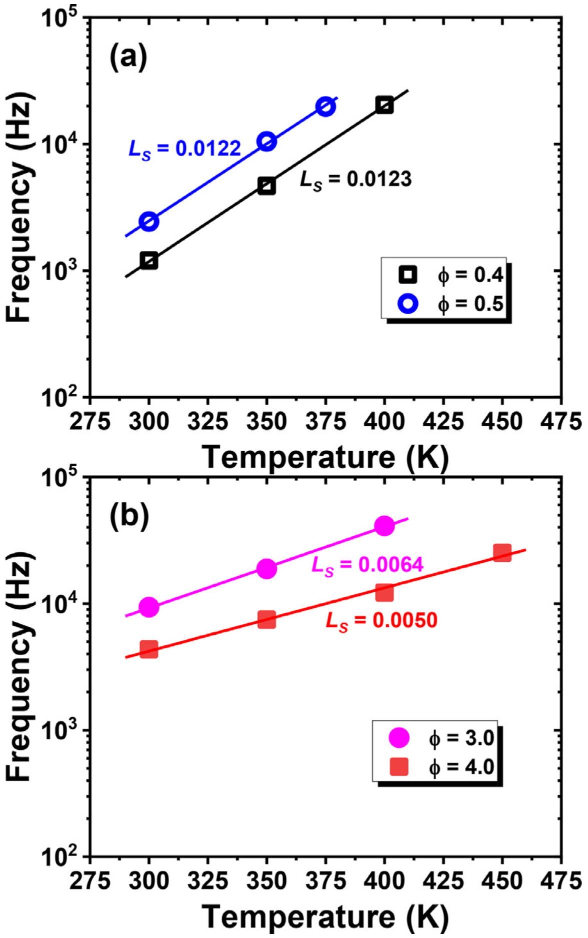

Fig. 18. Pulsating frequencies of the reaction front with different initial temperatures and equivalence ratios: (a) $\phi = 0.4$ and 0.5, (b) $\phi = 3.0$ and 4.0. $p_0 = 1$ atm. Line: linear fitted curves with the slopes of L_S.

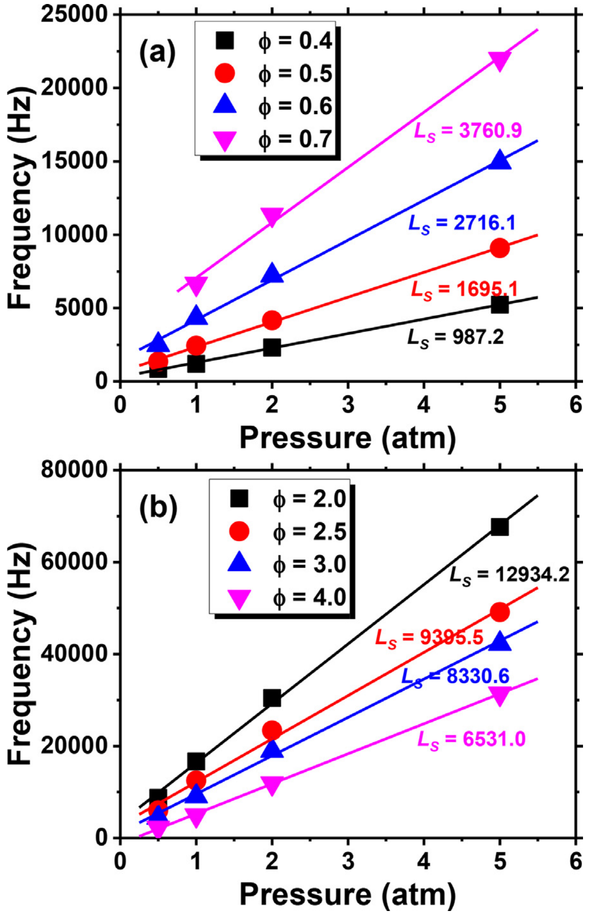

Fig. 19. Pulsation frequencies of the reaction front with different equivalence ratios and initial pressures. The initial temperature $T_0 = 300$ K. Line: linear fitted curves with the slopes of L_S.

computational diagnostic tool to identify the key combustion features through the eigen-analysis of local chemical Jacobian [38,67,68]. For the general chemically reacting system, the governing equation can be expressed as

$$\frac{D\boldsymbol{\varphi}}{Dt} = \mathbf{g}_{\omega}(\boldsymbol{\varphi}) + \mathbf{g}_{f}(\boldsymbol{\varphi}), \tag{10}$$

where $D(\cdot)/Dt$ is the material derivative and $\boldsymbol{\varphi}$ is the vector of local dependent variables, e.g. molar concentration and temperature. The symbol $\mathbf{g}_{\omega}(\boldsymbol{\varphi})$ is the vector of the chemical reaction source terms and $\mathbf{g}_{f}(\boldsymbol{\varphi})$ is the vector of the non-chemical terms, such as diffusion, mixing and compressibility in supersonic flows [68]. In CEMA, the chemical modes are associated with the eigenvalues of the chemical Jacobian matrix $\mathbf{J}$ of the local chemical reaction terms

$$\mathbf{J} = \frac{\partial \mathbf{g}_{\omega}(\boldsymbol{\varphi})}{\partial \boldsymbol{\varphi}}. \tag{11}$$

Among the eigenvalues of the chemical Jacobian matrix $\mathbf{J}$, the one with the maximal real part is denoted as $Re(\lambda_e)$. The local combustible mixture with the positive real part of eigenvalues $Re(\lambda_e) > 0$ is in the state of Chemical Explosive Mode (CEM), indicating the propensity of the mixture to auto-ignite, where λ_e is the first of the eigenvalues sorted in descending order with the real part. If $Re(\lambda_e) < 0$, it indicates post-ignition or non-reaction. $Re(\lambda_e) = 0$ corresponds to the ignition point or premixed reaction front.

Moreover, the terms $-\nabla \cdot \mathbf{q}$ and $\dot{\omega}_T$ in Eq. (3), which represent the thermal diffusion and chemical heat release respectively, are also analyzed to characterize the effects of chemical reaction and diffusion on the interactions between the shock and reaction fronts. It should be highlighted that the viscous heating ($\nabla \cdot [\mathbf{T} \cdot \mathbf{u}]$) in Eq. (3) is about 1% lower than the above two terms and therefore is not added in Figs. 20 and 21.

Figure 20 shows the results from CEMA and budget analysis of the energy equation at various instants within the detonation cycle discussed in Figs. 6–8. The instants t_1 and t_2 are in the accelerated decoupling stage (marked as “I” in Fig. 20a), whilst t_4 and t_5 in the accelerated coupling stage (marked as “II”). t_3 corresponds to a critical instant between two stages.

It is seen that, ahead of the shock front *SF*, the n-C_7H_{16}/air mixture is under non-CEM with $Re(\lambda_e) = 0$. The value of $Re(\lambda_e)$ begins greater than zero at the *SF* due to shock compression. $Re(\lambda_e)$ is greater than zero between the shock and reaction fronts in both accelerated decoupling and accelerated coupling stages. This suggests that the mixture between them is highly explosive and has propensity to be ignited. Behind the *RF*, $Re(\lambda_e)$ is less than zero, corresponding to post-ignition state. Note that there is a critical locus with $Re(\lambda_e) = 0$ at *RF*, indicating the transition between pre- and post-ignition states.

Furthermore, different variations of thermal diffusion ($-\nabla \cdot \mathbf{q}$) and reaction heat release ($\dot{\omega}_T$) can be observed with stages I and II. In the accelerated decoupling stage (i.e.t_1 and t_2), the thermal diffusion acts as sink term around the reaction front *RF*, and dominates over the heat release between *RF* and *SF*. However, they counterbalance each other between *RF* and *SF* at t_3. When the *RF* is accelerating towards the *SF* at t_4, thermal

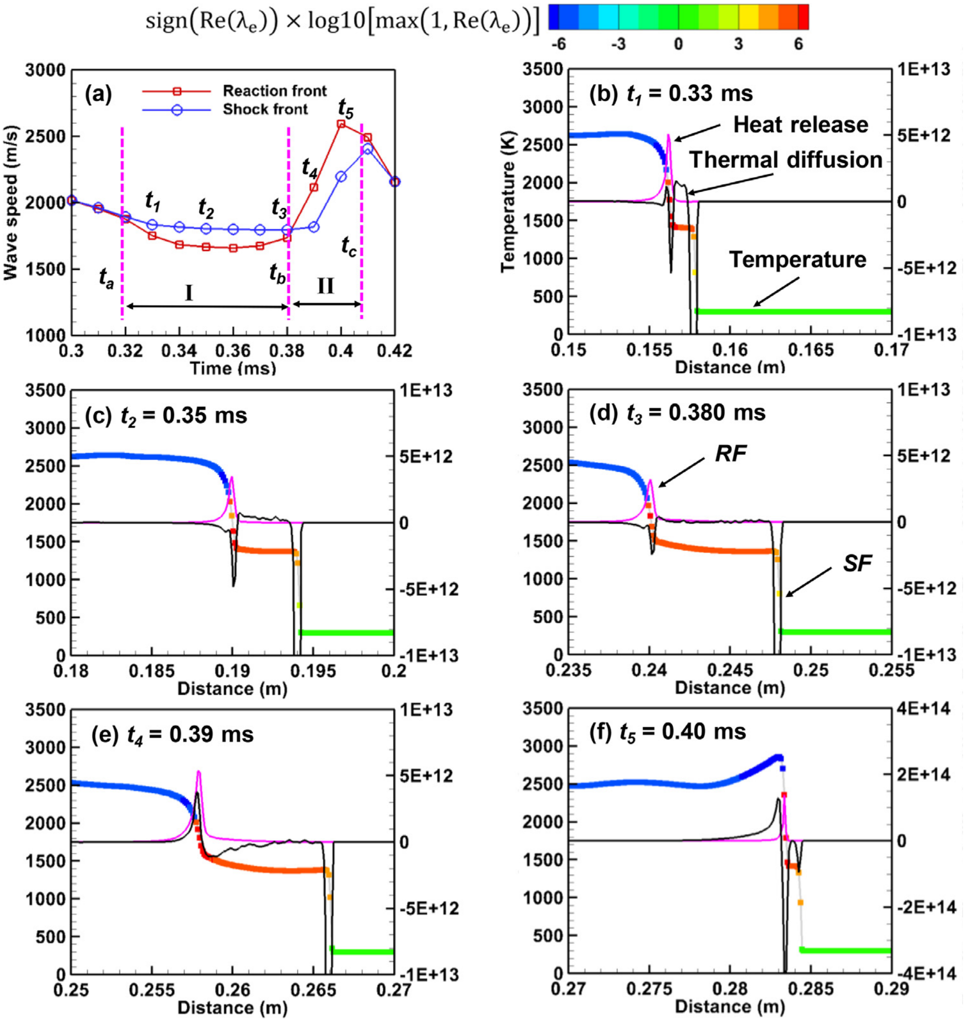

Fig. 20. (a) Time evolutions of reaction and shock propagation speeds with (ϕ, T_0, p_0) =(0.7,300 K, 1 atm) and (b–f) distributions of temperature and budgets of reaction heat release (in J/m^3/s) and thermal diffusion (J/m^3/s) in energy equation. The temperature profiles are colored by the logarithmic distribution of $Re(\lambda_e)$ from CEMA. *RF*: reaction front; *SF*: shock front.

diffusion, together with the reaction heat release, acts as source term around the *RF*. Therefore, the thermal diffusion may facilitate the formation of pressure bifurcation point *B1* in Fig. 6 and lead to *RF* acceleration towards the *SF*. Nevertheless, at t_5 (slightly before the second bifurcation point *B2*), negative thermal diffusion budget is seen around *RF*, which maybe induces their decoupling at a later instant. Therefore, thermal diffusion promotes decoupling and coupling of the two fronts in stages I and II, respectively, which can be confirmed by the numerical experiments in Appendix B.

Likewise, Fig. 21 shows the counterpart results for the fuel-rich case of $(\phi, T_0,\ p_0) = (3.0,\ 300\ \text{K},\ 1\ \text{atm})$ discussed in Figs. 11, 13 and 14. At t_1', the thermal diffusion contributes positively around the *RF*. When the *RF* is gradually decoupled from the leading *SF* (at t_2' and t_3'), considerable thermal diffusion occurs between the two fronts. In Fig. 20, the thermal diffusion is relatively small between *SF* and *RF*. At t_4' (slightly after the trifurcation point in Fig. 11), the thermal diffusion becomes stronger around the *RF*. This may enhance the *RF* and accelerated coupling occurs after t_4', as shown in Fig. 21(a). Similar to Fig. 20(f), the thermal diffusion acting as sink term can be observed around the *RF* at t_5' before detonation occurs.

The normalized contributions of species concentrations and temperature to a CEM are measured by evaluating the explosion index [38], $\mathbf{EI} = \frac{\text{diag}|\boldsymbol{a}_e\boldsymbol{b}_e|}{\sum(\text{diag}|\boldsymbol{a}_e\boldsymbol{b}_e|)}$, where "diag|·|" denotes the elementwise absolute values, and $\boldsymbol{a}_e$, $\boldsymbol{b}_e$ are the corresponding right and left eigenvectors of $Re(\lambda_e)$. Figures 22 and 23, respectively, show the distributions of EIs of important variables at two instants, respectively from accelerated decoupling and coupling stages (see Figs. 20a and 21a). In general, the distributions of the EIs show similar trends at these instants. Specifically, the radicals, e.g. HO_2, CH_2O and C_2H_4, are found to be the most important species (largest EI) to the CEM immediately behind the shock front, while temperature becomes dominant left to the red dashed lines (see Figs. 22 and 23), which represent the thermal runaway. It has been suggested that the local chemical reaction is dominated by autoignition if the radicals are dominant in the CEM, and is dominated by reaction front propagation if temperature plays an important role [38]. Therefore, the CEM in the induction zone consists of two parts: the autoignition dominated reaction immediately behind the shock front and the following propagating reaction front. Moreover, it is worth to note that HO_2 is the most important radical (largest EI) in the autoignition dominated reaction for both fuel-lean and fuel-rich cases, and its importance to CEM gradually decreases towards the thermal runaway process. In the autoignition dominated reaction, besides HO_2, CH_2O and C_2H_4 are also important in the fuel-lean and fuel-rich cases respectively, as indicated in Figs. 22 and 23.

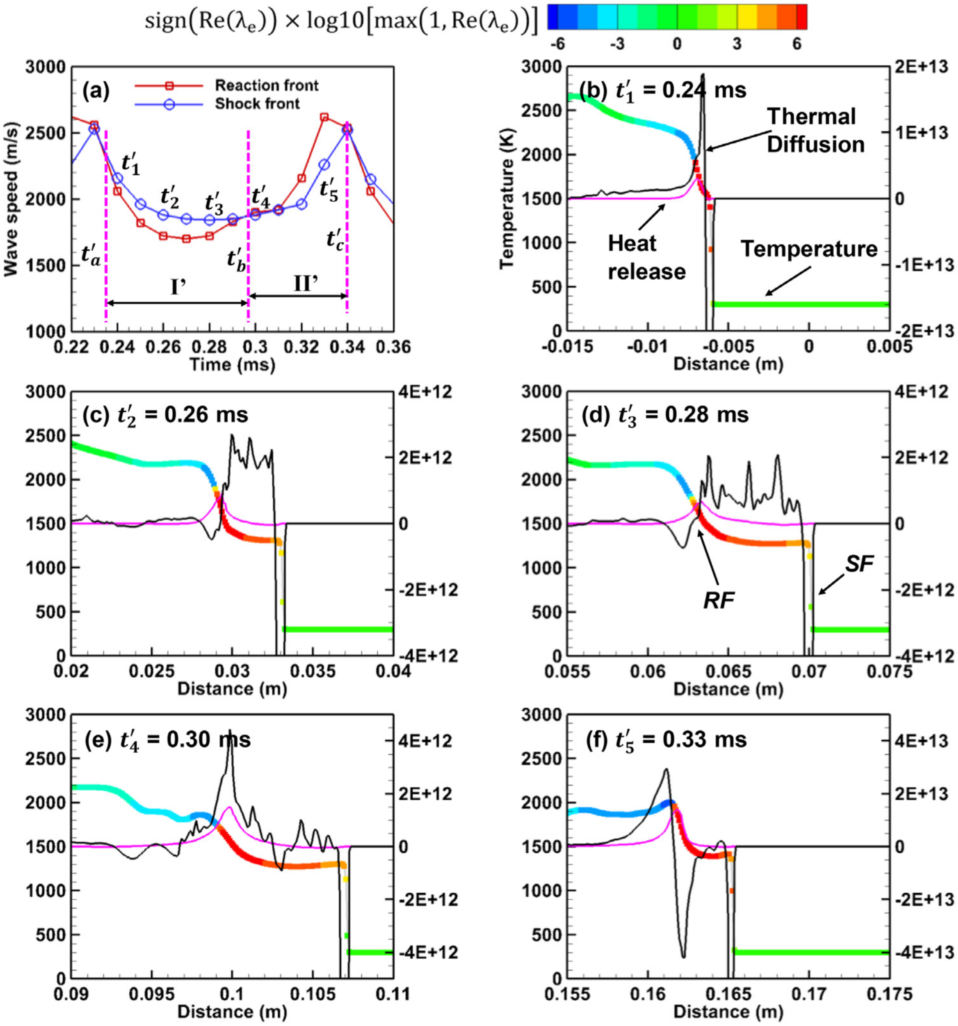

Fig. 21. (a) Time evolutions of reaction and shock propagation speeds with $(\phi, T_0, p_0) = (3.0, 300\ \text{K}, 1\ \text{atm})$ and (b–f) distributions of temperature and budgets of reaction heat release (in $\text{J/m}^3/\text{s}$) and thermal diffusion ($\text{J/m}^3/\text{s}$) in energy equation. The temperature profiles are colored by the logarithmic distribution of $Re(\lambda_e)$ from CEMA. *RF*: reaction front; *SF*: shock front

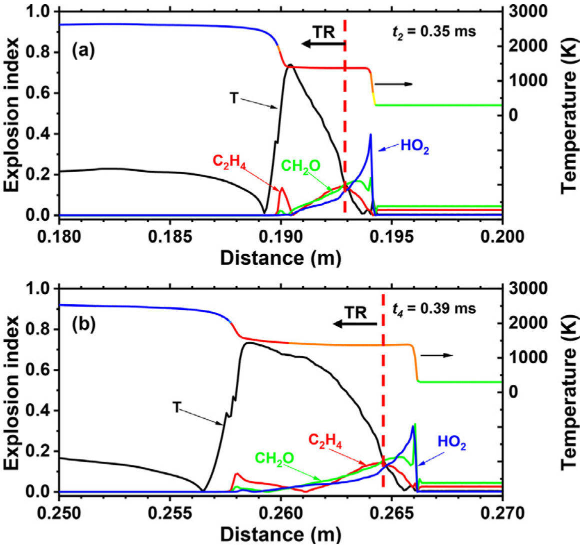

Fig. 22. Distributions of EIs of important variables at accelerated (a) decoupling and (b) coupling stages. $(\phi, T_0, p_0) = (0.7, 300\ \text{K}, 1\ \text{atm})$. TR: thermal runaway. The temperature profiles are colored by the logarithmic distribution of $Re(\lambda_e)$ and color bars are the same as in Fig. 20. (For interpretation of the references to colour in this figure legend, the reader is referred to the web version of this article.)

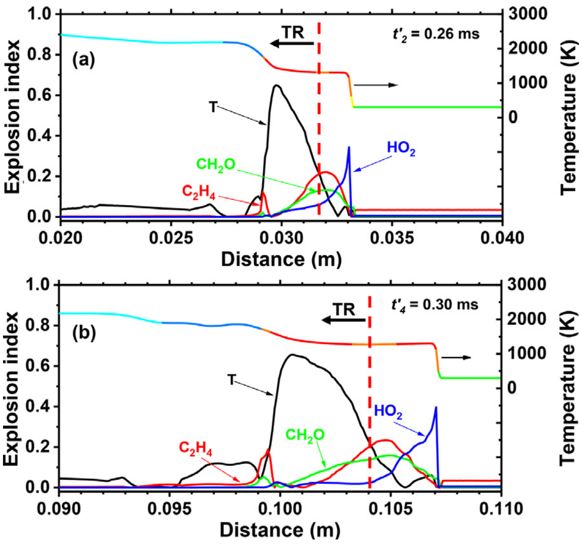

Fig. 23. Distributions of EIs of important variables at accelerated (a) decoupling and (b) coupling stages. $(\phi, T_0, p_0) = (3.0, 300\ \text{K}, 1\ \text{atm})$. TR: thermal runaway. The temperature profiles are colored by the logarithmic distribution of $Re(\lambda_e)$ and color bars are the same as in Fig. 20. (For interpretation of the references to colour in this figure legend, the reader is referred to the web version of this article.)

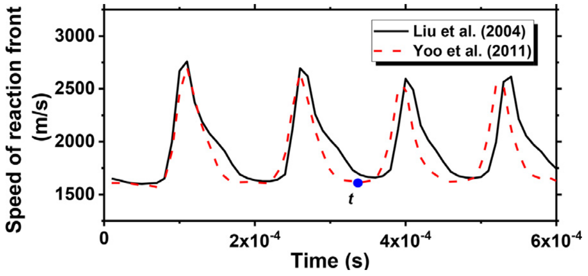

Fig. 24. Time history of reaction front propagation speed predicted with two skeletal mechanisms. $(\phi, T_0,\ p_0) = (0.7,\ 300\ \text{K},\ 1\ \text{atm})$. (For interpretation of the references to colour in this figure, the reader is referred to the web version of this article.)

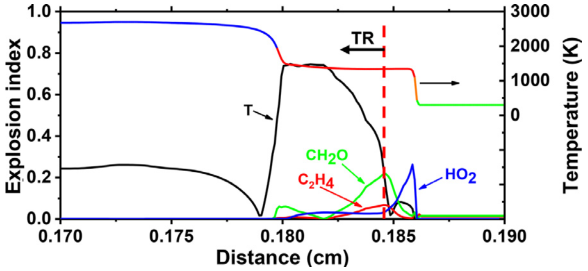

Fig. 25. Distributions of EIs of important variables at $t = 0.00034$ s (blue circle in Fig. 24) with reaction mechanism of Yoo et al. [70]. $(\phi, T_0,\ p_0) = (0.7,\ 300\ \text{K},\ 1\ \text{atm})$. TR: thermal runaway. The temperature profiles are colored by the logarithmic distribution of $Re(\lambda_e)$ from CEMA and color bars are same as in Fig. 20. (For interpretation of the references to colour in this figure legend, the reader is referred to the web version of this article.)

4.6. Sensitivity to chemical mechanism

The sensitivity of *n*-heptane pulsating detonation simulations to chemical mechanism is assessed by comparing the results from a one-step mechanism [69], the existing mechanism (44 species and 112 reactions, “44 s/112r”) [44] and a more detailed skeletal mechanism [70] (88 species and 387 reactions, “88 s/387r”). The initial condition of $(\phi, T_0,\ p_0) = (0.7,\ 300\ \text{K},\ 1\ \text{atm})$ is considered. It is observed (results not presented) that the pulsating detonation is not captured with the one-step mechanism. Instead, a steady propagation occurs with a constant propagation speed of about 1951 m/s. However, similar pulsating detonation propagation is observed when the 44 s/112r and 88 s/387r mechanisms are used. Figure 24 shows the time history of reaction front propagation speed predicted with two skeletal mechanisms. With both mechanisms, one predicts the same pulsating mode, i.e. single mode with low pulsating frequency, and periodic decoupling/coupling of the reaction and shock fronts. Nevertheless, there are still some differences. For instance, the pulsating frequency from the 88 s/387r mechanism is about 7217 Hz, which is slightly higher than that with the 44 s/112r mechanism, i.e. about 6667 Hz. This may be due to the different elementary reactions in these mechanisms.

The roles of the intermediate species in *n*-heptane pulsating detonations can be determined through comparing the explosion indices from CEMA. Figure 25 shows the EI distributions at $t = 0.00034$ s (blue circle in Fig. 24) with the 88 s/387r mechanism. HO_2, CH_2O and C_2H_4 are identified as the most important species to the CEM close to the shock front, while temperature becomes dominant near the reaction front. This is consistent with the results from the 44 s/112r mechanisms in Section 4.5. Similar radical EIs from two mechanisms can also be seen in the fuel-rich case of $\phi = 3.0$. The results in Figs. 24 and 25 indicate that: (1) radicals are important participants in pulsating *n*-heptane detonations and hence detailed mechanism is necessary; and (2) the predicted mechanisms and characteristic quantities of pulsating detonation in this work are not sensitive to various detailed mechanisms.

5. Conclusions

Pulsating instabilities of one-dimensional detonation propagation in off-stoichiometric *n*-heptane/air mixtures are simulated by solving reactive Navier−Stokes equations with a detailed chemical mechanism. The effects of equivalence ratio, initial pressure and temperature of the initial mixtures on pulsating detonations are studied.

The parametric studies show that the pulsating detonation in *n*-heptane/air mixtures is considerably affected by equivalence ratio. Pulsating detonation occurs when the equivalence ratio is less than 0.8 or greater than 1.5, whilst stable detonation is observed in near-stoichiometric mixtures. For the pulsating cases, single low-frequency pulsating mode is observed, and periodic decoupling / coupling occurs between the reaction front and shock front. In the decoupling period, the reaction front would undergo a DDT process and then develops into a new detonation wave. The DDT process is be affected by the equivalence ratio. For the fuel-lean cases, the heat release at the reaction front is dominated by the oxidation of small radicals, e.g. CO and OH, while for the fuel-rich cases, the heat release is dominated by oxidation of light hydrocarbon radicals, e.g. C_2H_4. In addition, the pulsating frequency exponentially varies with equivalence ratio and the closer to the stoichiometric condition the initial composition is, the higher the pulsating frequency is. It is also seen that the pulsating frequency increases linearly with initial pressure, but exponentially with initial temperature.

The chemical explosive mode analysis and budget analysis of the energy equation are conducted to identify the underpinning mechanism of pulsating detonation in *n*-heptane/air mixtures. The results suggest that the mixture between the reaction and shock fronts is highly explosive. Also, the thermal diffusion promotes decoupling and coupling of the two fronts in the accelerated decoupling and coupling stages, respectively. Moreover, the radicals, e.g. HO_2, CH_2O and C_2H_4, are found to be the most important radicals to the CEM close to the shock front, while temperature becomes dominant near the reaction front.

Declaration of Competing Interest

None.

Acknowledgments

The simulations were performed with the computational resources from National Supercomputing Center (NSCC) in Singapore (https://www.nscc.sg/). MZ and HZ are partially supported by the open research grant (No. KFJJ20-09M) from State Key Laboratory of Explosion Science and Technology, Beijing Institute of Technology. ZR is supported by National Natural Science Foundation of China (91841302). Wantong Wu from Tsinghua University is thanked for the assistance of CEMA calculations.

Appendix A. Effect of mesh resolution

In the present work, the mesh resolution is at least 60 cells per HRL. To quantitatively assess the effect of mesh resolution on detonation pulsating frequency, six cases with same initial temperature and pressure but with various equivalence ratios (0.5, 0.6, 0.7, 2.0, 2.5 and 3.0) are repeated with halved mesh size, i.e. the mesh resolution is greater than 120 cells/$L_{1/2}$, which leads to about 120 to 1420 cells/$L_{1/2}$ in different cases. Figure A1 shows that the pulsating frequency predicted with a halved mesh cell size is nearly the

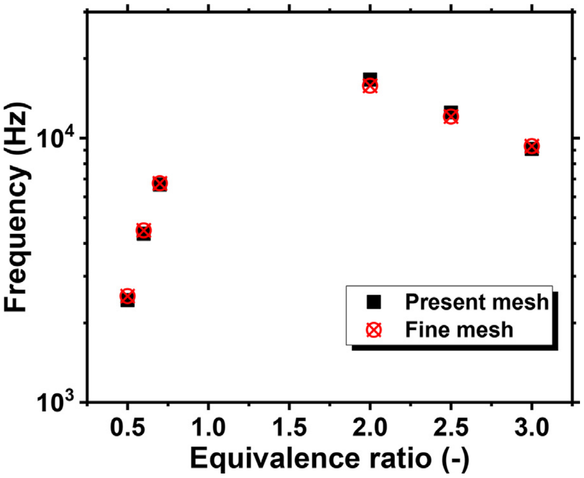

Fig. A1. Pulsation frequencies predicted with different mesh resolutions. $T_0 = 300\,\text{K}$ and $p_0 = 1$ atm.

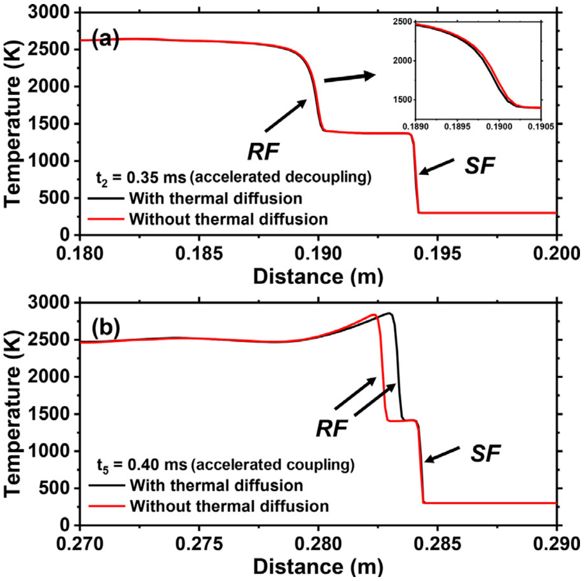

Fig. A2. Distributions of temperature with and without the thermal diffusion at accelerated (a) decoupling and (b) coupling stages. $(\phi, T_0,\ p_0) = (0.7,\ 300\ \text{K},\ 1\ \text{atm})$. *RF*: reaction front; *SF*: shock front.

same as the results obtained with the present resolution, and the maximum error is less than 3% for all cases. Therefore, the present resolution is sufficient for *n*-heptane pulsating detonation simulations.

Appendix B. Effect of thermal diffusion

To confirm the thermal diffusion effects on pulsating detonation, two cases with $(\phi, T_0,\ p_0) = (0.7,\ 300\ \text{K},\ 1\ \text{atm})$ and $(\phi, T_0,\ p_0) = (3.0,\ 300\ \text{K},\ 1\ \text{atm})$ are repeated without thermal diffusion. Figure A2 shows the distributions of temperature with and without thermal diffusion at two instants with $(\phi, T_0,\ p_0) = (0.7,\ 300\ \text{K},\ 1\ \text{atm})$. Here the two instants (t_2 and t_5 in Fig. 20a) are from the accelerated decoupling and accelerated coupling stages, respectively. It can be seen that the thermal diffusion has limited effects on the reaction front propagation in the accelerated decoupling stage (see Fig. A2a), in which the thermal diffusion only slightly decreases the propagation speed of the reaction front. However, in the accelerated coupling stage, the reaction front is significantly accelerated when thermal diffusion is considered (see Fig. A2b), which leads to faster approaching the leading shock front. Also, the shock front propagation is almost not affected by thermal diffusion in both stages. Also, the thermal diffusion does not change pulsating detonation mode, i.e. single mode with low pulsating frequency, but the pulsating frequency would increase when thermal diffusion is not included. Similar tendencies are also observed with $(\phi, T_0,\ p_0) = (3.0,\ 300\ \text{K},\ 1\ \text{atm})$, which is not shown here for brevity.

References

[1] Y.B. Zeldovich, On the theory of the propagation of detonation in gaseous systems, National Advisory Committee for Aeronautics, Washington, DC, United States, 1950 Report No. NACA-TM-1261.
[2] J. Von Neuman, Theory of detonation waves, Institute for Advanced Study, Princeton NJ, 1942.
[3] W. Döring, On detonation processes in gases, Ann. Phys. 43 (1943) 9.
[4] J. Buckmaster, J. Neves, One-dimensional detonation stability: the spectrum for infinite activation energy, Phys. Fluids 31 (1988) 3571–3576.
[5] A. Bourlioux, A.J. Majda, V. Roytburd, Theoretical and numerical structure for unstable one-dimensional detonations, SIAM J. Appl. Math. 51 (1991) 303–343.
[6] A.A. Vasil'Ev, V.V. Mitrofanov, M.E. Topchiyan, Detonation waves in gases, Combust. Explos. Shock Waves 23 (1987) 605–623.
[7] P. Clavin, L. He, Stability and nonlinear dynamics of one-dimensional overdriven detonations in gases, J. Fluid Mech. 306 (1996) 353–378.
[8] P. Clavin, L. He, F.A. Williams, Multidimensional stability analysis of overdriven gaseous detonations, Phys. Fluids 9 (1997) 3764–3785.
[9] L. He, Theoretical determination of the critical conditions for the direct initiation of detonations in hydrogen-oxygen mixtures, Combust. Flame 104 (1996) 401–418.
[10] S. Yungster, K. Radhakrishnan, Pulsating one-dimensional detonations in hydrogen–air mixtures, Combust. Theory Model. 8 (2004) 745–770.
[11] M. Short, G.J. Sharpe, Pulsating instability of detonations with a two-step chain-branching reaction model: theory and numerics, Combust. Theory Model. 7 (2003) 401–416.
[12] C. Leung, M.I. Radulescu, G.J. Sharpe, Characteristics analysis of the one-dimensional pulsating dynamics of chain-branching detonations, Phys. Fluids 22 (2010) 126101.
[13] W. Han, C. Wang, C.K. Law, Pulsation in one-dimensional H2–O2 detonation with detailed reaction mechanism, Combust. Flame 200 (2019) 242–261.
[14] W. Han, W. Ma, C. Qian, J. Wen, C. Wang, Bifurcation of pulsation instability in one-dimensional H 2– O 2 detonation with detailed reaction mechanism, Phys. Rev. Fluids 4 (2019) 103202.
[15] C. Campbell, D.W. Woodhead, CCCCI, The ignition of gases by an explosion-wave. Part I. Carbon monoxide and hydrogen mixtures, J. Chem. Soc. 129 (1926) 3010–3021.
[16] J.J. Erpenbeck, Stability of steady-state equilibrium detonations, Phys. Fluids 5 (1962) 604–614.
[17] J.J. Erpenbeck, Stability of idealized one-reaction detonations, Phys. Fluids 7 (1964) 684–696.
[18] J.J. Erpenbeck, Nonlinear theory of unstable one-dimensional detonations, Phys. Fluids 10 (1967) 274–289.
[19] W. Fickett, W.W. Wood, Flow calculations for pulsating one-dimensional detonations, Phys. Fluids 9 (1966) 903–916.
[20] H.I. Lee, D.S. Stewart, Calculation of linear detonation instability: one-dimensional instability of plane detonation, J. Fluid Mech. 216 (1990) 103–132.
[21] L. He, J.H.S. Lee, The dynamical limit of one-dimensional detonations, Phys. Fluids 7 (1995) 1151–1158.
[22] G.J. Sharpe, S. Falle, One-dimensional numerical simulations of idealized detonations, Proc. R. Soc. Lond. Ser. A Math. Phys. Eng. Sci. 455 (1999) 1203–1214.
[23] G.J. Sharpe, Linear stability of idealized detonations, Proc. R. Soc. Lond. Ser. A Math. Phys. Eng. Sci. 453 (1997) 2603–2625.
[24] J.B. McVey, T.Y. Toong, Mechanism of instabilities of exothermic hypersonic blunt-body flows, Combust. Sci. Technol. 3 (1971) 63–76.
[25] Y. Daimon, A. Matsuo, Detailed features of one-dimensional detonations, Phys. Fluids 15 (2003) 112–122.
[26] A. Matsuo, T. Fujiwara, Numerical investigation of oscillatory instability in shock-induced combustion around a blunt body, AIAA J. 31 (1993) 1835–1841.
[27] P. Clavin, F.A. Williams, Dynamics of planar gaseous detonations near Chapman-Jouguet conditions for small heat release, Combust. Theory Model. 6 (2002) 127–139.
[28] A. Matsuo, K. Fujii, Numerical investigation of the one-dimensional piston supported detonation waves, Energy Convers. Manag. 38 (1997) 1283–1295.
[29] M. Short, J.J. Quirk, On the nonlinear stability and detonability limit of a detonation wave for a model three-step chain-branching reaction, J. Fluid Mech. 339 (1997) 89–119.
[30] M. Short, A nonlinear evolution equation for pulsating Chapman–Jouguet detonations with chain-branching kinetics, J. Fluid Mech. 430 (2001) 381–400.
[31] H.D. Ng, M.I. Radulescu, A.J. Higgins, N. Nikiforakis, J.H.S. Lee, Numerical investigation of the instability for one-dimensional Chapman–Jouguet detonations with chain-branching kinetics, Combust. Theory Model. 9 (2005) 385–401.

[32] C.M. Romick, T.D. Aslam, J.M. Powers, Verified and validated calculation of unsteady dynamics of viscous hydrogen–air detonations, J. Fluid Mech. 769 (2015) 154–181.

[33] M.I. Radulescu, H.D. Ng, J.H.S. Lee, B. Varatharajan, The effect of argon dilution on the stability of acetylene/oxygen detonations, Proc. Combust. Inst. 29 (2002) 2825–2831.

[34] M.A. Sussman, Numerical simulation of shock-induced combustion, Stanford University, 1995 PhD thesis.

[35] Y. Daimon, A. Matsuo, Unsteady features on one-dimensional hydrogen-air detonations, Phys. Fluids 19 (2007) 116101.

[36] V. Anand, E. Gutmark, Rotating detonation combustors and their similarities to rocket instabilities, Prog. Energy Combust. Sci. 73 (2019) 182–234.

[37] G.D. Roy, S.M. Frolov, A.A. Borisov, D.W. Netzer, Pulse detonation propulsion: challenges, current status, and future perspective, Prog. Energy Combust. Sci. 30 (2004) 545–672.

[38] T.F. Lu, C.S. Yoo, J.H. Chen, C.K. Law, Three-dimensional direct numerical simulation of a turbulent lifted hydrogen jet flame in heated coflow: a chemical explosive mode analysis, J. Fluid Mech. 652 (2010) 45–64.

[39] B.J. McBride, Coefficients for calculating thermodynamic and transport properties of individual species, National Aeronautics and Space Administration, Office of Management, 1993.

[40] B.E. Poling, J.M. Prausnitz, J.P. O'connell, The properties of gases and liquids, Mcgraw-hill, New York, 2001.

[41] https://blog.nus.edu.sg/huangwei/nus-ryrhocentralfoam-solver/, 2020.

[42] H. Jasak, Error analysis and estimation for the finite volume method with applications to fluid flows, Imperial College London, London, UK, 1996 PhD Thesis.

[43] E. Harier, G. Wanner, Solving ordinary differential equations II: stiff and differential algebraic problems, Springer Verlag., 1991.

[44] S. Liu, J.C. Hewson, J.H. Chen, H. Pitsch, Effects of strain rate on high-pressure nonpremixed n-heptane autoignition in counterflow, Combust. Flame 137 (2004) 320–339.

[45] C. Qi, P. Dai, H. Yu, Z. Chen, Different modes of reaction front propagation in n-heptane/air mixture with concentration non-uniformity, Proc. Combust. Inst. 36 (2017) 3633–3641.

[46] P. Dai, Z. Chen, X. Gan, Autoignition and detonation development induced by a hot spot in fuel-lean and CO2 diluted n-heptane/air mixtures, Combust. Flame 201 (2019) 208–214.

[47] M. Zhao, H. Zhang, Modelling rotating detonative combustion fueled by partially pre-vaporized n-heptane sprays, Phys. Fluids (2020) Submitted for publication.

[48] C.J. Greenshields, H.G. Weller, L. Gasparini, J.M. Reese, Implementation of semi-discrete, non-staggered central schemes in a colocated, polyhedral, finite volume framework, for high-speed viscous flows, Int. J. Numer. Methods Fluids 63 (2010) 1–21.

[49] H. Zhang, M. Zhao, Z. Huang, Large eddy simulation of turbulent supersonic hydrogen flames with OpenFOAM, Fuel 282 (2020) 118812.

[50] M. Zhao, J.-.M. Li, C.J. Teo, B.C. Khoo, H. Zhang, Effects of variable total pressures on instability and extinction of rotating detonation combustion, Flow Turbul. Combust. 104 (2020) 261–290.

[51] H.Z. Zhiwei Huang, Majie Zhao, Yong Xu, Guangze Li, Eulerian-Lagrangian modelling of detonative combustion in two-phase gas-droplet mixtures with OpenFOAM, Fuel 286 (2020) 119402.

[52] M. Zhao, H. Zhang, Origin and chaotic propagation of multiple rotating detonation waves in hydrogen/air mixtures, Fuel 275 (2020) 117986.

[53] L.F. Gutiérrez Marcantoni, J. Tamagno, S. Elaskar, rhoCentralRfFoam: an OpenFOAM solver for high speed chemically active flows – simulation of planar detonations, Comput. Phys. Commun. 219 (2017) 209–222.

[54] L.F. Gutiérrez Marcantoni, J. Tamagno, S. Elaskar, Two-dimensional numerical simulations of detonation cellular structures in H2O2Ar mixtures with OpenFOAM®, Int. J. Hydrogen Energy 42 (2017) 26102–26113.

[55] S. Yungster, K. Radhakrishnan, Structure and stability of one-dimensional detonationsin ethylene-air mixtures, Shock Waves 14 (2005) 61–72.

[56] J. Lawson, J. Shepherd, Shock and detonation toolbox installation instructions, California Institute of Technology, Pasadena, CA, 2019.

[57] J.E. Shepherd, Detonation in gases, Proc. Combust. Inst. 32 (I) (2009) 83–98.

[58] H. Ng, A. Higgins, C. Kiyanda, M. Radulescu, J. Lee, K. Bates, N. Nikiforakis, Nonlinear dynamics and chaos analysis of one-dimensional pulsating detonations, Combust. Theory Model. 9 (2005) 159–170.

[59] H. Wei, C. Chen, G. Shu, X. Liang, L. Zhou, Pressure wave evolution during two hotspots autoignition within end-gas region under internal combustion engine-relevant conditions, Combust. Flame 189 (2018) 142–154.

[60] R.L. Alpert, T.Y. Toong, Periodicity in exothermic hypersonic flows about blunt projectiles, Astronaut. Acta 17 (1972) 539–560.

[61] A. Matsuo, K. Fujii, Computational study of large-disturbance oscillations in unsteady supersonic combustion around projectiles, AIAA J. 33 (1995) 1828–1835.

[62] G.J. Sharpe, S. Falle, One-dimensional nonlinear stability of pathological detonations, J. Fluid Mech. 414 (2000) 339–366.

[63] W. Fickett, W.C. Davis, Detonation, University of California Press, Berkeley, CA, 1979, p. 17.

[64] J.P. Saintcloud, N. Manson, C. Guerraud, C. Brochet, Some peculiaritimes of very unstable detonations in gaseous mixtures, Astronaut. Acta 17 (1972) 487.

[65] W. Cao, H.D. Ng, J.H.S. Lee, Near-limit detonations of methane–oxygen mixtures in long narrow tubes, Shock Waves (2020) 1–7, doi:10.1007/s00193-020-00940-5.

[66] G.J. Sharpe, S. Falle, Numerical simulations of pulsating detonations: I. Nonlinear stability of steady detonations, Combust. Theory Model. 4 (2000) 557–574.

[67] C. Xu, J.-.W. Park, C.S. Yoo, J.H. Chen, T. Lu, Identification of premixed flame propagation modes using chemical explosive mode analysis, Proc. Combust. Inst. 37 (2019) 2407–2415.

[68] W. Wu, Y. Piao, Q. Xie, Z. Ren, Flame diagnostics with a conservative representation of chemical explosive mode analysis, AIAA J. 57 (2019) 1355–1363.

[69] C.K. Westbrook, F.L. Dryer, Simplified reaction mechanisms for the oxidation of hydrocarbon fuels in flames, Combust. Sci. Technol. 27 (1981) 31–43.

[70] C.S. Yoo, T. Lu, J.H. Chen, C.K. Law, Direct numerical simulations of ignition of a lean n-heptane/air mixture with temperature inhomogeneities at constant volume: parametric study, Combust. Flame 158 (2011) 1727–1741.